Ultrasonic Classification of Emboli

A thesis submitted in partial fulfillment of the requirement
for the degree of Bachelors of Science in Physics from
The College of William and Mary

by

Alison M. Pouch

Accepted for _____Honors _____

_____
Dr. Gina Hoatson, Director

_____
Dr. Mark Hinders, Advisor

_____
Dr. Christopher Del Negro

_____
Dr. Robert Welsh

Williamsburg, VA
May 2, 2007

Contents

Abstract …….. 1

Introduction …… 2

Chapter 1: Ultrasound Instrumentation and Imaging Basics ……. 4

1.1 Ultrasound and Acoustic Impedance ……... 4

1.2 Ultrasound Instrumentation ……. 5

1.3 Automated Scanning and Imaging ……... 6

1.4 Experimental Imaging and Signal Processing ……. 7

Chapter 2: Clinical Application of the Emboli Detection and Classification System ……. 14

Chapter 3: The Emboli Detection and Classification System in Experiment …….. 18

3.1 Experimental Specifications …….. 18

3.2 The EDAC System Display ……..…….. 18

3.3 The Experimental Circuit ……... 20

Chapter 4: Frequency-Domain Analysis of an Analytical Scattering Model ……..…. 23

4.1 Analytical Scattering Model ……..…. 23

4.2 Frequency-Domain Analysis ……..…… 26

4.3 Testing of Material Parameters ……..……. 34

4.4 Scattering Effects of a Thin Layer Surround the Embolus ……..... 40

Chapter 5: Time-Domain Analysis and Simulation Comparison …… 43

5.1 Analytical Time-Domain Analysis …… 43

5.2 Comparison of Analytical and FDTD Approaches ……... 44

Chapter 6: Sizing Gaseous Microemboli ……. 49

6.1 Theoretical and Experimental Verification of Gaseous Embolus Sizing …….. 49

6.2 Phase Analysis ……..……...… 53

Chapter 7: Viscous-Fluid Model Analysis ……..…. 56

Chapter 8: Acoustic Radiation Force Calculations …….……. 61

Chapter 9: Discussion …….……. 71

Acknowledgements …….……. 74

References …….……... 74

Appendix A: Scattering Coefficients for the Viscous-Fluid Model …… 76

Appendix B: Code for Functions Implemented in MATLAB …….…… 78

Abstract

The goal of this thesis is to develop theoretical verification for a system that uses broadband ultrasonic pulses to characterize microemboli in cardiopulmonary bypass (CPB) circuits. This Emboli Detection and Classification (EDAC^{TM}: Luna Innovations Incorporated, Roanoke, VA)) device non-invasively tracks and classifies individual microemboli passing through extracorporeal circuits. To determine the size and composition of microemboli in the bloodstream, we begin by implementing an analytical ultrasound scattering model in MATLAB. Our frequency- and time-domain analyses are then compared to a two-dimensional scattering model based on the cylindrical acoustic finite integration technique (CAFIT), assuming axisymmetric wave propogation. Confirmed by experimental data from the EDAC device, the analytical model and CAFIT simulations indicate a linear relationship between the amplitude of backscattered echoes and diameter of gas microemboli. We extend our analytical model to account for viscosity in the microembolus and surrounding fluid, which necessitates consideration of both compressional and shear wave modes. The result, a more complicated scattering solution, will assist in better characterizing non-gaseous microemboli. Our scattering solutions are the basis for an exact analytical model to calculate the radiation force on emboli needed to optimize debubbling adjuncts to the EDAC device.

Introduction

In this study, the frequency-domain and time-domain analysis of ultrasound scattering from fluid spheres is applied to emboli classification. An embolus (pl. emboli) refers to a microbubble, generally of gas or lipid composition, that flows through the bloodstream. Presenting a significant health hazard, these emboli may occlude blood vessels and thereby prevent the flow of blood to surrounding tissue and vital organs. Such embolic events are of significant concern in cardiac and orthopedic surgery, commercial and military diving expeditions, high-altitude operations, and other military objectives and medical scenarios. Luna Innovations, Inc. is currently developing an ultrasonic emboli detection and classification (EDAC) device, shown in Figure 1.1, to be used as a tool for noninvasive and nondestructive examination of debris in the body's vasculature.

Figure 1.1 The EDAC device developed by Luna Innovations, Inc.

The first chapter of this thesis provides an overview of the basics of ultrasound technology, including automated scanning instrumentation and foundations of imaging. In addition, it outlines experimental projects that were conducted in William and Mary's Nondestructive Evaluation (NDE) lab to demonstrate techniques in ultrasound imaging and signal processing. The second chapter explains the clinical application of the EDAC device and its use in cardiopulmonary bypass (CPB) circuits. The experimental specifications of the EDAC device are introduced in the third chapter, along with a description of the EDAC system display and experimental circuit used to test the device. In the fourth chapter, we outline the analytical scattering model that is the basis of our frequency-domain scattering analysis. The chapter includes an analysis of material parameters and the effects a thin shell surrounding the embolus has on backscatter. In the fifth chapter, we use our analytical model to develop a time-domain scattering analysis and test the result against a two-dimensional, axisymmetric ultrasound scattering simulation based on a variant of the finite difference time domain (FDTD) technique. The sixth chapter presents a scheme for sizing gas microemboli and describes the results of a phase analysis. The seventh chapter introduces a viscous-fluid model that extends our original analytical formulation. Acoustic radiation force calculations are presented in chapter eight, and a concluding discussion follows in chapter nine.

Chapter 1: Ultrasound Instrumentation and Imaging Basics

1.1 Ultrasound and Acoustic Impedance

Sound in a fluid (liquid or gas) produces a wave or a series of small fluctuations manifested by changes in a material's pressure and density. Sound audible to humans lies within the frequency range of 20 Hz to 20 kHz. Sound above a frequency of 20 kHz is referred to as ultrasound. Ultrasound is extremely useful in medical diagnostics, as its applications provide a real-time, non-ionizing, noninvasive, portable, and relatively inexpensive means of imaging anatomy.

Acoustic impedance is a critical concept in ultrasound technology; it impacts the design of ultrasound transducers and the assessment of sound absorption in a medium. The acoustic impedance of a given material is defined as the product of its density and acoustic velocity. This factor must be taken into account when considering the transmission and reflection of ultrasonic pulses at the boundary of two different materials. The impedances of two materials can be used, as follows in Equation 1.1, to determine the reflection coefficient R at the boundary of two materials:

$$R = \left[\frac{(Z_2 - Z_1)}{(Z_2 + Z_1)}\right]^2 \tag{1.1}$$

In this expression, $Z_1 = \rho_1 c_1$ and $Z_2 = \rho_2 c_2$, where Z is acoustic impedance, ρ is the material's density, and c is the acoustic velocity in a given material. It is evident that larger impedance mismatches result in larger reflection coefficients. Large values of R, in turn, correspond to strong echoes, indicative of greater amounts of reflected energy returned from a boundary between two materials.

1.2 Ultrasound Instrumentation

All ultrasound instrumentation incorporates several fundamental components, including a transducer, a pulser-receiver, and a computer or scope display.

A transducer is a device that converts energy from one form to another; in this case, electrical energy to acoustic energy and vice versa. Specifically, piezoelectric transducers (PZTs) utilize the piezoelectric effect to perform this conversion. The transducer's active element consists of a piece of polarized material, which changes shape when an electric field is applied. The polarized molecules align themselves with the induced voltage, thus changing the material's structural dimensions. Conversely, an electric field is generated when the material changes shape as a result of applied pressure. Figure 1.2 illustrates the basic structure of a typical acoustic piezoelectric transducer. The PZT disk, the active transducer element, consists of piezoelectric ceramics, whose thickness determines the frequency of the transducer and the wavelength of an outgoing pulse. A thin PZT element vibrates with a wavelength that is twice its thickness; thus, the thickness of a particular PZT disc is half the desired radiated wavelength. Two electrodes connected across the PZT element allow an electric field to be induced and generated by the element. Behind the PZT disk, the damping material suppresses initial vibrations of the element, while the matching layer on the opposite side of the disk prevents the impedance of ultrasonic emissions from the transducer.

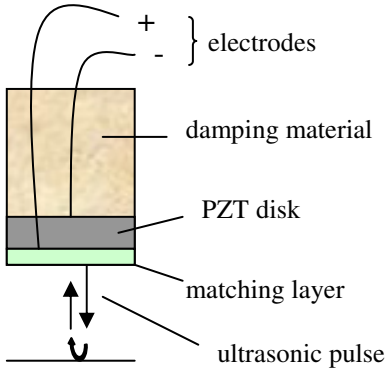

Figure 1.2 Basic structure of an acoustic piezoelectric transducer.

The pulser-receiver serves as a link between the display and transducer. The pulser in a pulser-receiver generates short, large amplitude electric pulses to the transducer. It controls both pulse length and pulse energy. In the receiver section of the instrument, the voltage signals produced by the transducer, after being received as ultrasonic pulses reflected from the scatterer, are amplified. This provides the output for the digital display or signal processing. In addition, the receiver is responsible for signal rectification, filtering returned signals, gain, and reject control.

Electric information returned from the transducer provides data for the display, which can produce a variety of visual images of the anatomy under investigation.

1.3 Automated Scanning and Imaging

Ultrasonic scanning systems are used for automated data acquisition and imaging. As opposed to hand-held transducers, these automated systems emit and receive ultrasonic pulses at regular, controlled intervals while moving the transducer between pulses. They are particularly useful for scanning material defects. An example of the typical scan layout for a flat surface is shown in Figure 1.3. In this case, the transducer travels along the scanning path above and parallel to the specimen's surface. At each point in the scan configuration, the signal strength and/or the signal's travel time are measured. These values, in turn, are plotted using varying color schemes or shading to produce detailed images of the material's features.

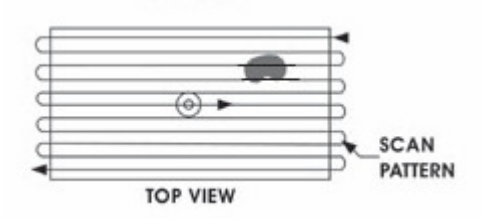

(a)

(b)

Figure 1.3 (a) Top view of a typical scan configuration for a flat specimen. The transducer travels above and parallel to the specimen and at each point measures the strength of the signal returned from the material. (b) A side view of the transducer scanning a flat specimen.

Water immersion tanks are commonly used in laboratory ultrasound scanning systems. Both the transducer and specimen to be scanned are submerged in water. The water maintains consistent coupling as the transducer passes above the material in the desired configuration.

Automated scanning systems are often capable of displaying ultrasound data in three of the most common image formats: A-scan, B-scan, and C-scan presentations, which correspond to A-mode, B-mode, and C-mode, respectively. The A-scan is a waveform with the echo amplitude plotted as a function of time. Since sound speed is relatively constant, the time delay, indicated on the horizontal axis of the A-scan, corresponds to the depth of the reflection.

The B-scan presentation represents an anatomic cross-section in the scanning plane. The travel time of the ultrasonic pulses is displayed along the vertical axis, and the distance from the transducer to each reflecting interface is plotted along the horizontal axis. B-scan images correspond to brightness mode, in which the brightness of each point, or pixel, is determined by the strength of the echo. A B-scan is usually produced by setting a trigger gate on the corresponding A-scan; when the signal amplitude is great enough to trigger the gate, a point is

produced on the B-scan. Real-time instruments produce multiple cross-sectional images per second. Since the rapid sequence of frames provides a continuously changing image, real-time automated systems provide immediate and convenient acquisition of the desired image.

The C-scan presentation represents an image whose plane is parallel to that of the transducer's scanning path. To produce the C-scan display, a data collection gate is established on the A-scan. As the signal amplitude is recorded at regular intervals along the scanning path, the relative signal amplitude is represented as a color or shade of gray for each position where data was received. A C-scan can portray the features that reflect sound within or on either surface of the test piece.

Similar to brightness mode, presentations in M-mode assign a spot brightness for each echo voltage returned from the reflector. This, in turn, produces a two-dimensional recording of reflector position (motion) versus time.

1.4 Experimental Imaging and Signal Processing

Research in William and Mary's Nondestructive Evaluation (NDE) lab began with projects intended to develop experience with ultrasound instrumentation and the process of generating and interpreting images using experimental data. First the GE RT 5000 medical ultrasound illustrated in Figure 1.4 was used to generate and interpret typical brightness-mode images generated in a medical setting. Next, a variety of automated scans were conducted using a water immersion tank in the NDE lab.

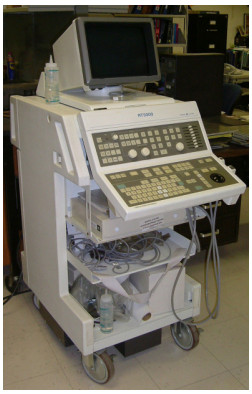

Figure 1.4 GE RT 5000 in William and Mary's NDE lab.

Figure 1.5 illustrates the instrumentation used in the automated scan experimental setup: the immersion tank, transducer, motor controller, the UTEX pulser-receiver, digital display (Windows NT Workstation 4.00), and the specimen being evaluated. The first four scans evaluated defects of increasing complication in aluminum plates. The final two scans were of a Susan B. Anthony Dollar coin and a William & Mary logo impressed in a metal plate.

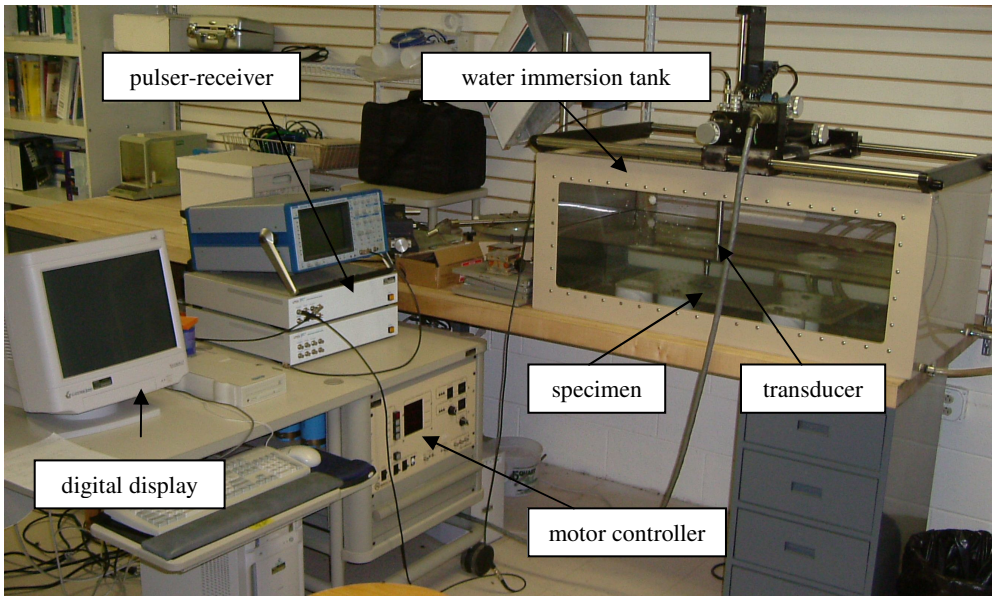

Figure 1.5 Experimental setup for the automated tank scans. The specimen and transducer are submerged in the water tank so that the water provides consistent coupling for the emission and reflection of ultrasonic waves. The motor controller is externally triggered by the computer to control the scan configuration, while the pulser-receiver is responsible for producing and receiving electric pulses from the transducer. The data is loaded into MATLAB, which is used to generate images using the experimental data.

The same basic procedure was followed for each of the tank scans. First, the Labview ASCAN program was used to determine the starting position and number of data points collected at each position. The motor controller was used to position the transducer above the defect, while the pulser-receiver was externally triggered by the computer to record the waveform amplitude at specified points. Once the desired waveforms were isolated using ASCAN and the appropriate gate was established, Labview's CSCAN program was utilized to size the scan configuration. Each tank scan was set up to collect data for a square surface area in increments of 101 by 101 steps in the horizontal plane. Once this scan was completed, the data was compiled in MATLAB as a three dimensional array, specifying the transducer's position along the x-y plane and the echoes received at each point. MATLAB was then used to view specific A-scans, B-scans, and C-scans using the collected data. The codes implemented in MATLAB used to generate these images are presented in Appendix A. Table 1.1 provides a description of each scan specimen and the transducer used for each scan. C-scan images from the final two tank scans are presented in Figures 1.6 and 1.7.

Scan Specimen	Date of Scan	Transducer	Gate Specifications	Diagram of Specimen
Plate 10: Single Ring	6/02/05	5 MHz, 2″ focal length	start: 6400 number: 800 SEP: 6000 x 6000 SSS: 60 x 60 SR: 100 MHz	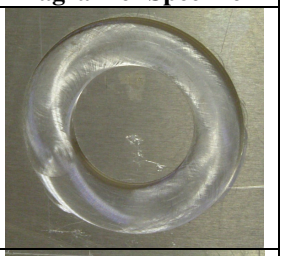
Plate 20: Swirls (plate inverted)	6/02/05	5MHz, 2″ focal length	start: 6400 number: 800 SEP: 8000 x 8000 SSS: 80 x 80 SR: 100 MHz	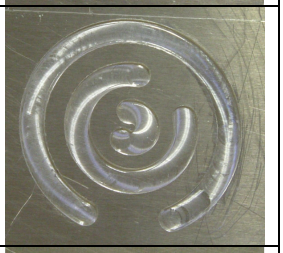
Plate 5: Multiple Rings (plate inverted)	6/03/05	10 MHz, 4″ focal length	start: 6400 number: 800 SEP: 6000 x 6000 SSS: 60 x 60 SR: 100 MHz	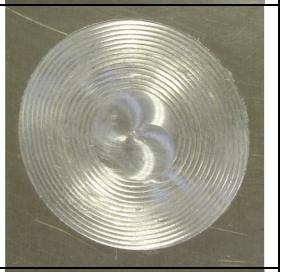
Plate 14: Irregularly Incremented Steps	6/03/05 6/06/05	20 MHz, 1″ focal length, focused	start: 11450 number: 800 SEP: 13000 x 13000 SSS: 130 x 130 SR: 100 MHz	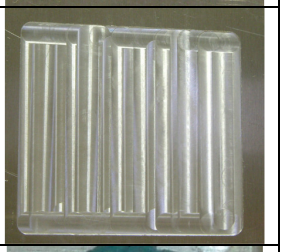
Susan B. Anthony Dollar	6/07/05	25 MHz, 1″ focal length, focused	start: 400 number: 500 SEP: 3000 x 3000 SSS: 30 x 30 SR: 130 MHz	
W&M Logo	6/08/05	20 MHz, 1″ focal length, focused	start: 3400 number: 700 SEP: 11000 x 11000 SSS: 110 x 110 SR: 100 MHz	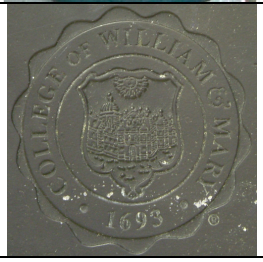

Table 1.1 Specifications for the six automated scans conducted using the water immersion tank in William and Mary's NDE lab. Gate specifications are denoted as follows: *start* refers to the starting position on the A-scan, *number* refers to the number of data points taken beyond the starting position, SEP is the scan end position in the x-y plane, SSS is the scan step size in the x- and y-directions, and SR is the sampling rate.

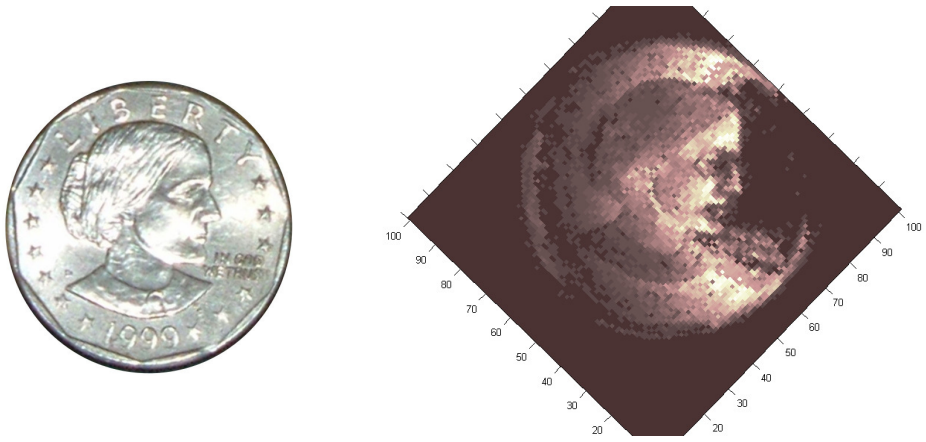

(a) (b)

Figure 1.6 (a) Susan B. Anthony Dollar coin scanned using a 25 MHz transducer in a water immersion tank. (b) Corresponding C-scan generated using MATLAB. The year of the coin (1999) is faintly apparent beneath Anthony's profile.

(a) (b)

Figure 1.7 (a) William and Mary logo impressed in a metal plate. This specimen was scanned using a 20 MHz transducer in a water immersion tank. (b) Corresponding C-scan generated using MATLAB.

For practice in signal processing, the same automated scanning system was used to capture A-scans of ultrasound pulses reflected from the flat end of a solid brass cylinder submerged in water. Piezoelectric transducers in the frequency range of 1-30 MHz were used in these experiments. The MATLAB Filter Design and Analysis Tool was used to create low-pass and band-pass filters to filter high-frequency noise from the reflected waveforms. Fast Fourier transforms were used to generate accurate frequency spectra of the returned waves. The same signal processing techniques were applied to "snippets"— reflected waveforms obtained with the EDAC device when monitoring the flow of air bubbles through an experimental circuit. This practice in signal processing helped to effectively use MATLAB to perform Fourier transforms, inverse fast Fourier transforms, convolutions, and filtering with Butterworth, Chebyshev Type 1 and 2, and Elliptic filters.

Chapter 2: Clinical Application of the Emboli Detection and Classification (EDAC) System

Cardiopulmonary bypass (CPB) is a form of extracorporeal circulation that temporarily takes over the function of heart and lungs during various surgical operations. CPB circuits are frequently used in open-heart surgery, when beating of the muscle must be arrested so that chambers in the heart can be opened. CPB circuits are additionally used in hemodialysis. Figure 2.1 provides a basic illustration of the flow of blood from the body through the heart-lung machine and back into systemic circulation.

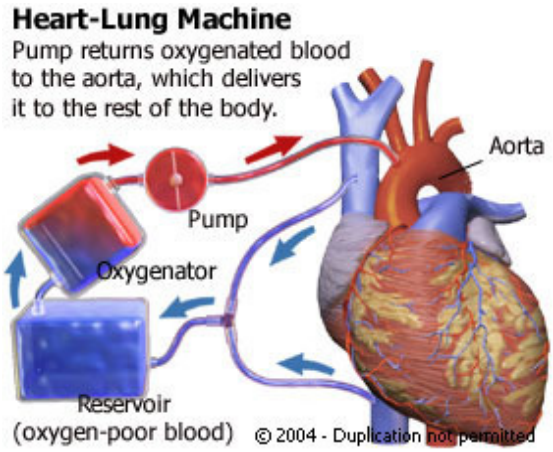

Figure 2.1 Illustration of the heart-lung machine, a device used in cardiopulmonary bypass surgery to temporarily oxygenate and pump blood while the heart is arrested. Image adapted from http://www.biomed.brown.edu/.../HeartLungMachine.jpg.

CPB circuits are frequently used in coronary artery bypass grafting (CABG), the most common type of open-heart surgery in the United States, with more than 500,000 surgeries performed each year [1]. CABG is a treatment for coronary artery disease, occurring when the arteries supplying blood to the heart muscle become blocked due to plaque buildup in one or more vessels. As illustrated in Figure 2.2, a healthy artery or vein from another part of the body is grafted to the blocked artery, providing a new route for oxygen-rich blood to pass to the heart muscle.

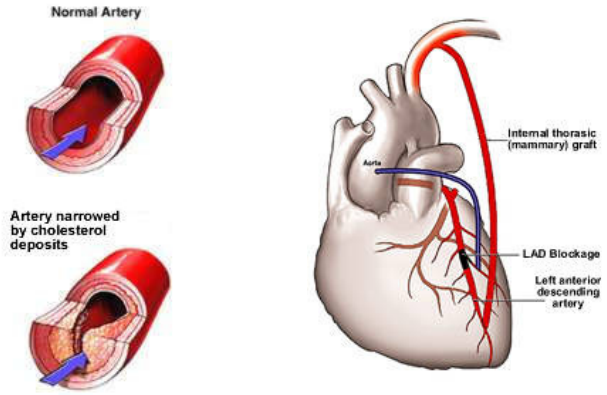

Figure 2.2 Illustration of normal and partially-blocked arteries (left), and diagram of a coronary artery bypass graft (right). Image adapted from http://www.ehealthmd.com/library/cardiacbypass/CB_whatis.html.

During this surgery, it is typical for gas bubbles to originate in the extracorporeal tubing, becoming infused with fluids that reenter systemic circulation. These bubbles may appear when preparing the line for use or may be produced as a result of turbulent flow in the CPB tubing. Since warming initiates bubble formation, the gas emboli may form as a result of active blood warming systems that serve to mediate changes in fluid temperature. For 15 to 40% of the population that has a cardiac right-to-left shunt (as a result of a patent foramen ovale or other anatomic anomaly), it would be likely for a gas bubble to pass from the venous to arterial circulation, and on to the brain or coronary arteries during or after surgery. Such bubbles are responsible for the most serious of gas embolic events— massive brain ischemia and stroke or myocardial ischemia and infarction (heart attack). Gas microemboli present the additional risk of increasing clotting in the bloodstream by activating coagulation and inducing platelet aggregation [2].

Numerous studies over the past 20 years have shown a relationship between increased embolic load delivered to the brain and neurocognitive deficits [3-5]. These studies have led to

increasing use of arterial line filters in the CPB circuit, as recommended in a recent review paper [6]. Increased use of arterial line filters provides better patient protection, but there is still room for improvement, as stated in Barak and Katz's recent review article (2005):

> The filter pores are 28 to $40 \cdot 10^{-6}$ m (28 to 40 μm), allowing smaller emboli to pass through. Nevertheless, larger air and fat emboli also pass through and enter the circulation downstream to the filter whenever their load is high. Microbubbles that traverse the filter join and become large bubbles.

Thus, even with the inclusion of arterial line filters, it is important to monitor embolic load both pre- and post-filter. Pre-filter monitoring provides the operating team advance warning as the arterial filter accumulates emboli in its pores. Such a warning allows the team to eliminate sources of emboli before the filter becomes saturated and releases emboli into the patient. A second channel post-filter provides feedback on the effectiveness of those procedures.

To provide these capabilities, the EDAC system employs a series of broadband ultrasound pulses with a center frequency of 4 MHz to detect and track microemboli in CPB circuits. This is in contrast to narrowband Doppler ultrasound systems, which have been used extensively for over 25 years to detect gas emboli in the blood flow. Over this time, many advances in Doppler emboli detection technology have been reported, including systems that digitize and display the Doppler shifted signal for ease of counting [7], automatically derive an emboli grade [8], or automatically derive an emboli count [9-10]. None of these advances address a fundamental limitation of narrowband detection, which is they do not provide the resolution necessary to differentiate *one* bubble from many bubbles. The broadband EDAC can automatically track and display (depth versus time) an *individual* bubble and count it as one, even while numerous faster bubbles flow past it. Count rates exceeding 1000 emboli/sec have

been regularly observed with the EDAC, although it is impossible to benchmark these counts against another device.

Accurate counts of emboli, however, do not provide a complete picture as larger emboli are more significant clinically than smaller emboli. Thus, it is desirable to weigh each count according to the size of the microemboli. It is additionally critical to distinguish embolic composition (gas, lipid, clot, etc.) in order to better identify the source of debris during surgery. These capabilities are particularly needed: Roach and colleagues have calculated an annual $400 million as the additional cost of in-hospital neurologic morbidity after cardiac surgery. A true estimate of costs, including long-term rehabilitative services for neurocognitive deficits, likely results in additional expenditures of $2 to $4 billion annually [2].

Chapter 3: Experimental Specifications, EDAC Display, and Experimental Circuit

3.1 Experimental Specifications

A basic illustration of the experimental setup is illustrated in Figure 3.1. A piezoelectric transducer in pulse-echo mode is positioned on an angle block at 30º with respect to the blood flow. With a center frequency of 3.9 MHz and 80% bandwidth, the broadband transducer emits a transmit signal with a 1-cm beam width. Due to these transducer specifications, a frequency range of 2 to 6 MHz is considered in our analysis. The relevant emboli in this study range in size from 20 to several hundred microns in diameter and pass approximately 1 cm in front of the transducer face, placing the scatterers within the transducer's near field. Since the application of the EDAC device is to monitor blood flow through extracorporeal circuits, an *in vitro* experimental setup is considered.

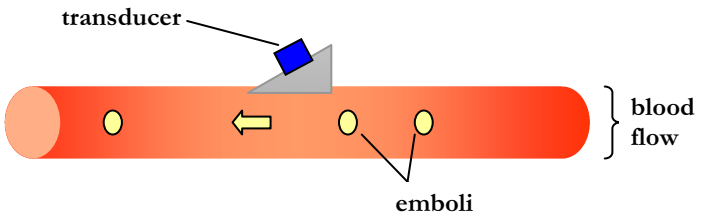

Figure 3.1 A basic diagram of the experimental setup, not drawn to scale. The pulse-echo transducer emits an ultrasonic wave and receives the reflection from emboli in the blood flow.

3.2 The EDAC System Display

In Phase I of this emboli detection research, Luna designed an EDAC system to process the pulse-echo signal returned from artifacts in the bloodstream. A typical EDAC screen display is presented in Figure 3.2. The top, large section of the screen is a time-motion display in B-mode. In this screen, the individual embolus tracks are identified with boxes marking the beginning and end of each track. The horizontal axis is the depth or range; it indicates distance

from the transducer, increasing from left to right. The vertical axis marks time, increasing from top to bottom. The bottom left window of the screen shows an A-scan, a single echo extracted from an embolus trace. To the right of this window, the system settings and embolus counts are presented. In the right bottom corner, there is a histogram showing the count total and classification for each second within a 2.5-minute time period.

The horizontal axis of the time-motion display illustrates a depth of 1.5 cm beyond the starting point, and one screen shot covers 0.5 seconds along the vertical axis. The relative velocity of the emboli can be determined from the curvature of their traces. As the emboli travel under the transducer, they move closer to the transducer element and cause perturbations in the returned A-scan lines. If an embolus slows, the depth or range does not change significantly, and the trace appears relatively vertical. Faster moving emboli likewise create near-horizontal traces since their distance from the transducer decreases quickly. The goal in the emboli classification phase of the project is to evaluate the experimental data in A-mode and identify a relationship between a backscattered waveform and the scatterer's material properties.

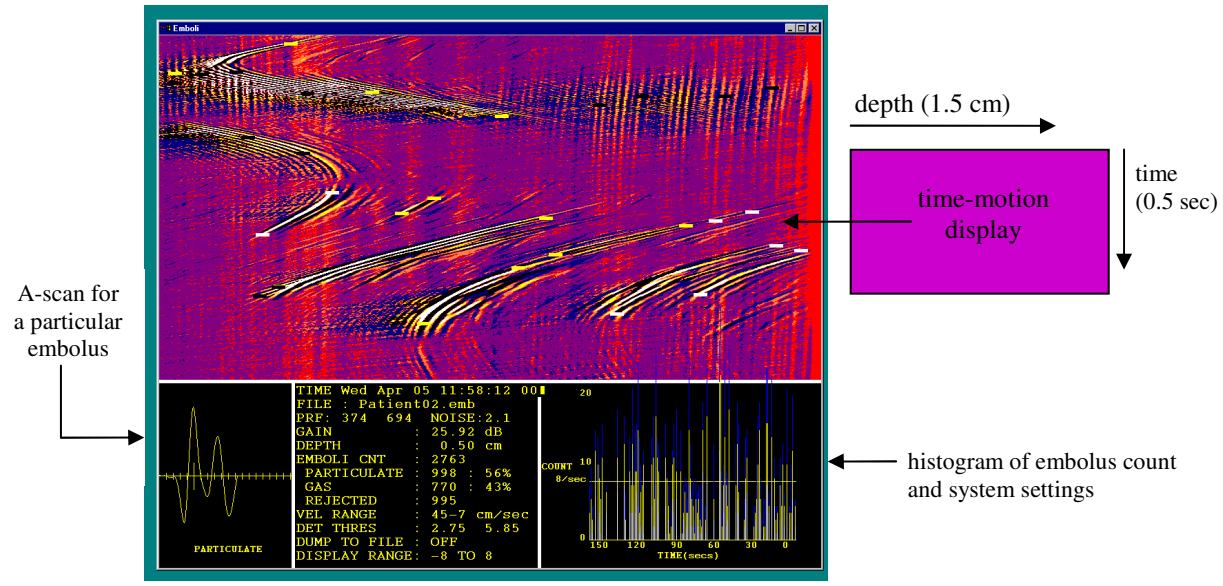

Figure 3.2 Typical screenshot of EDAC, Luna's Emboli Detection and Classification system. The time-motion display shows individual embolus paths, marked at beginning and end by small white and yellow boxes. The program provides embolus counts and the relative velocities of emboli flowing through the bloodstream. In the lower left corner, the A-scan of a particular embolus is shown, a waveform that will be compared to theoretical models of ultrasonic backscattering to determine the size and composition of the individual embolus.

3.3 The Experimental Circuit

The experimental circuit designed and tested in the Luna laboratory in Hampton, VA is illustrated in Figure 3.3. The test circuit employed a blood-mimicking fluid made of glycerine, water, and trace amounts of NaN_3 flowing in standard 0.95-cm diameter PVC tubing. A roller-type cardiovascular perfusion pump (Cobe Cardiovascular, Arvada, CO) was used to pump the glycerine mixture through the circuit. A custom micropipette bubble injector was inserted into the circuit after the pump and the microbubbles were detected through polycarbonate connector windows inserted into the circuit. The first window was used for optical detection of the microemboli, while an EDAC probe was attached to the second window for ultrasonic detection. The injected microemboli were then removed from the circuit using a tall graduated cylinder followed by a Polypure Capsule 10 μm filter (Pall Corporation, East Hills, NY). The tall graduated cylinder removed large bubbles in which the buoyant force of the bubble was sufficient to overcome downward flow within the cylinder, while the filter removed smaller bubbles that passed through the cylinder.

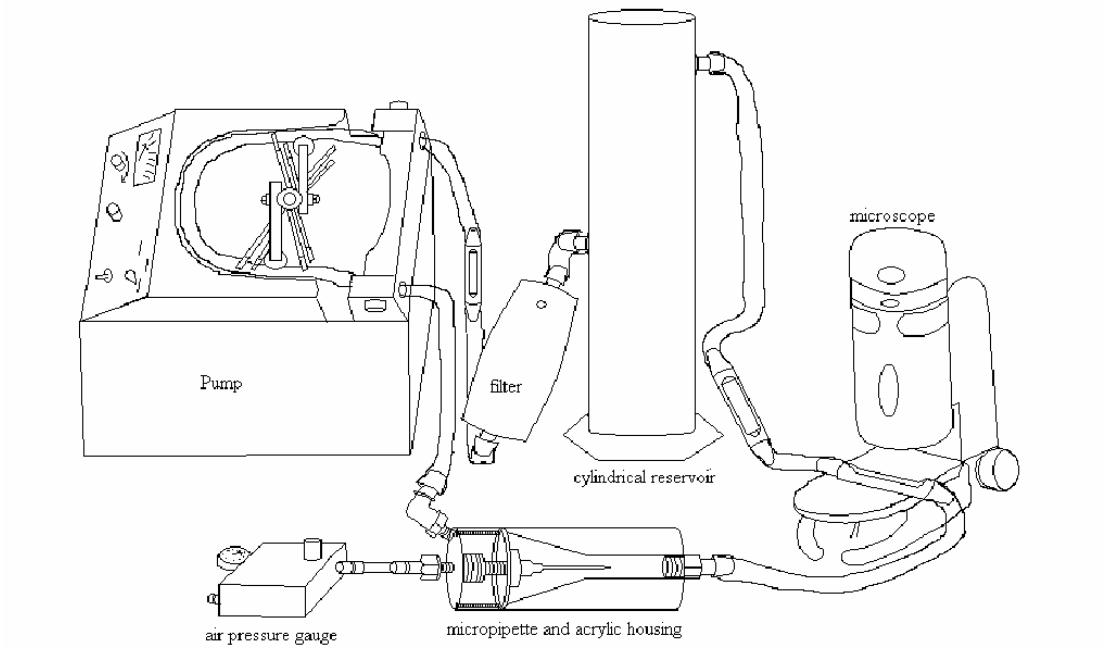

Figure 3.3 Diagram of the bubble circuit used in initial testing of the EDAC system. The bubbles and fluid would flow counter-clockwise in this circuit.

Strobing an LED while acquiring microscopic images in the movie mode enabled capture of fast-moving bubbles on a host computer for later analysis. Example images are shown in Figure 3.4.

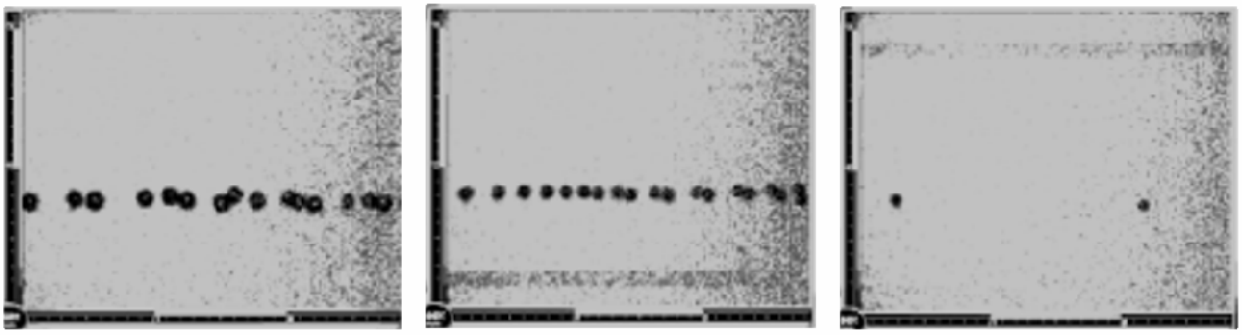

Figure 3.4 Examples of images acquired with the USB microscope while strobing an LED to capture fast-moving bubbles. In all the images, a 1 micron micropipette tip was used to inject bubbles into the circuit, with the air pressure set to 2.07 x 105 Pa for the left image, 1.72 x 105 Pa for the middle image, and 1.38 x 105 Pa for the right image.

In a second set of circuit studies, the USB microscope was replaced with a TM1400 Monochrome CCD Camera (PULNIX, Copenhagen, Denmark) with 1392 x 1040 resolution and a 30 frame per second transfer rate. The CCD camera was equipped to capture the images for analysis on a standard PC (Dell Corporation, Austin, TX). As with the USB microscope, the emboli were illuminated through the backside of the optical transmission cell. The camera was also equipped to yield 10 micron coverage for a single image pixel. All images were taken with a 1/2000th sec. shutter speed and an aperture setting of F4 to resolve fast-moving microemboli. The resolution of the camera was validated using plastic microspheres of known size (100 micron). Figure 3.5 illustrates CCD images processed using a custom MATLAB routine. In step 1 each succeeding images were subtracted from their preceding frame (step 1a and step 1b) to yield a difference image (step 2) free of background clutter such as tube walls. In step 3, a detection threshold was set and the frame searched for pixel clusters below the detection threshold. The number of adjacent pixels in a cluster was used to size each microemboli, using the formula 1 pixel = 10 microns.

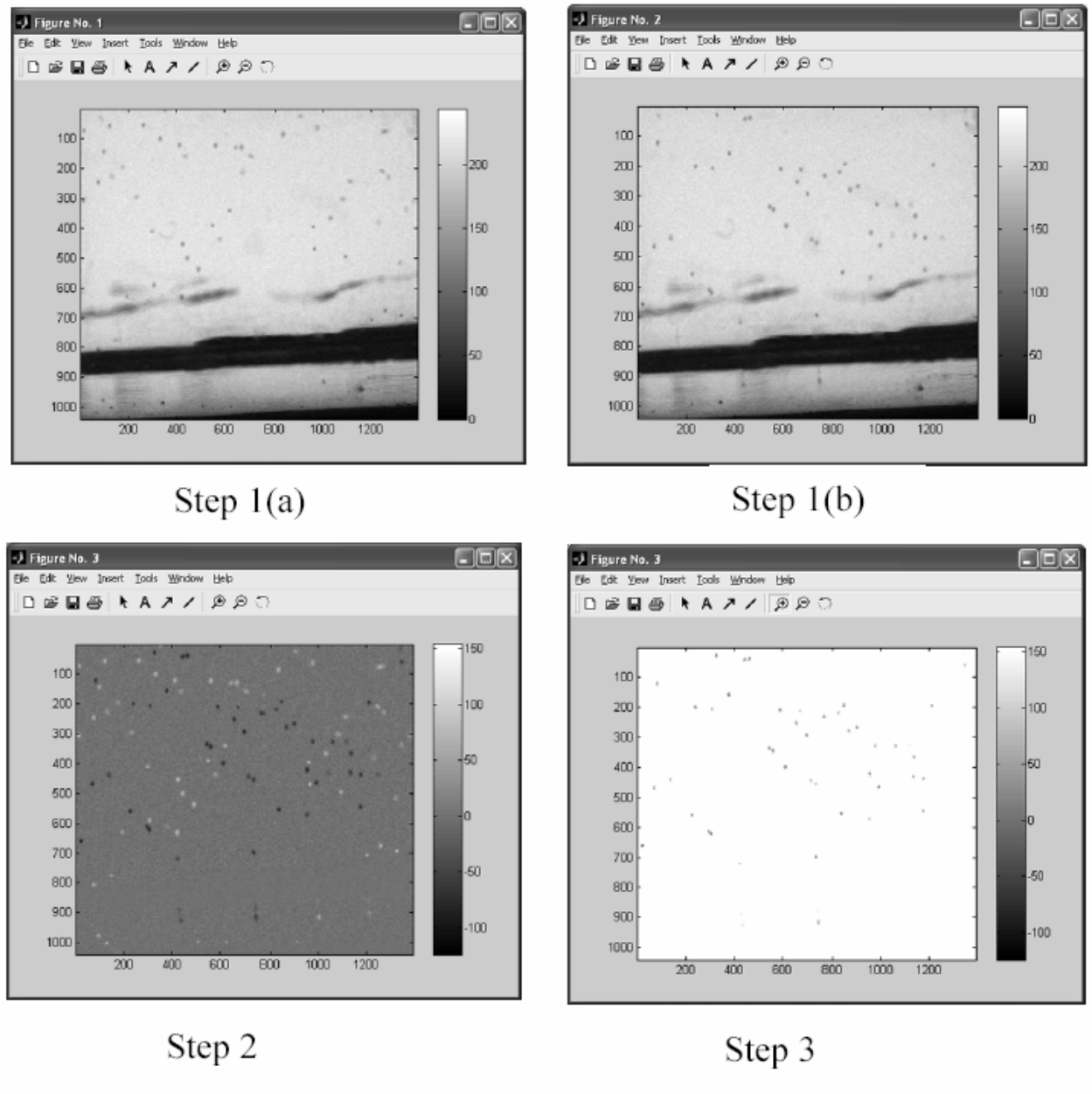

Figure 3.5 CCD images processed using a custom MATLAB routine.

Chapter 4: Frequency-Domain Analysis of an Analytical Scattering Model

4.1 Analytical Scattering Model

The first objective is develop a theoretical model of ultrasound scattering in order to evaluate the inverse problem of determining the size and composition of individual spherical scatterers from a backscattered signal. We specifically aim to quantify embolus size and distinguish gas emboli from fat and clot-like emboli. We initially assume that, as fluid scatterers, gas and fat bubbles do not support shear waves. V.C. Anderson's analytical solutions in *Sound Scattering from a Fluid Sphere* [11] are employed as the foundation of our theoretical model. Anderson's eigenfunction expansions have been utilized in a number of parallel applications, including mechanical characterization of microparticles in suspension [12] and the study of acoustic scattering by individual gas-bearing zooplankton [13]. Here we use Anderson's exact steady-state solutions to interpret experimental data of ultrasound scattering from spherical particulates in blood flow through extracorporeal circuits.

In *Sound Scattering from a Fluid Sphere* [11], V.C. Anderson formulates the following problem: A fluid sphere of radius a located at the origin of the spherical coordinate system is surrounded by an infinite fluid whose acoustical properties generally differ from those of the sphere. Let k' be the wave number of the scatterer and k the wave number of the surrounding medium. A plane acoustic wave of angular frequency ω and pressure amplitude $\wp_0$ travels parallel to the polar axis and impinges upon the sphere, giving rise to internal wave p' and external spherical wave p. These waves, including the incident acoustic wave p_o, may be expanded in spherical harmonics, where the sinusoidal time dependence is of the form $e^{-i\omega t}$:

$$p_0 = \wp_0 \sum_{m=0}^{\infty} (-i)^m (2m+1) P_m(\mu) j_m(kr) e^{-i\omega t} \tag{4.1}$$

$$p' = \sum_{m=0}^{\infty} B_m P_m(\mu) j_m(k'r) e^{-i\omega t}, \quad r < a \tag{4.2}$$

$$p = \sum_{m=0}^{\infty} A_m P_m(\mu) [j_m(kr) + i y_m(kr)] e^{-i\omega t}, \quad r > a \tag{4.3}$$

Here P_m is the Legendre function, $\mu = \cos\theta$, and j_m and n_m are spherical Bessel functions of the first and second kinds, respectively. The coefficients of the spherical harmonics are determined by applying boundary conditions across the surface of the scatterer and ensuring that the acoustic pressure of the spherical wave p satisfies the three-dimensional wave equation. The following boundary conditions account for continuity of acoustic pressure and radial velocity across the scatterer's surface:

$$p(a) + p_0(a) = p'(a), \tag{4.4}$$

$$u_r(a) + u_{0,r}(a) = u_r'(a).$$

Here p is acoustic pressure and u_r is the radial component of the particle velocity. Solving these equations for A_m, the amplitude of the external wave p may be expressed as

$$A_m = \frac{-\wp_0 (-i)^m (2m+1)}{(1 + iC_m)}, \tag{4.5}$$

where C_m is the following expression of spherical Bessel functions and their derivatives:

$$C_m = \frac{\left[\frac{\alpha_m(k'a)}{\alpha_m(ka)}\right]\left[\frac{y_m(ka)}{j_m(k'a)}\right] - \left[\frac{\beta_m(ka)}{\alpha_m(ka)}\right]gh}{\left[\frac{\alpha_m(k'a)}{\alpha_m(ka)}\right]\left[\frac{j_m(ka)}{j_m(k'a)}\right] - gh}, \tag{4.6}$$

$$\alpha_m = (2m+1)\frac{\partial[j_m(ka)]}{\partial(ka)} = mj_{m-1}(ka) - (m+1)\,j_{m+1}(ka),$$

$$\beta_m = (2m+1)\frac{\partial[y_m(ka)]}{\partial(ka)} = my_{m-1}(ka) - (m+1)y_{m+1}(ka).$$

In these expressions, g is the relative density ρ'/ρ and h is the relative acoustic speed c'/c.

The pressure of the scattered wave at any point outside the spherical scatterer is

$$p = -\wp_0 \sum_{m=0}^{\infty}\left[\frac{(-i)^m(2m+1)}{(1+iC_m)}\right] \times P_m(\mu)[j_m(kr) + iy_m(kr)]e^{-i\omega t}. \tag{4.7}$$

Anderson proceeds to define a reflectivity factor R, the ratio of the amplitude of the scattered wave p to the geometric cross-section $p_{geom} = a/2r$, assuming axial symmetry. For the special case of backscatter ($\theta = 0$), the reflectivity is expressed as

$$R = \frac{2}{ka}\left|\sum_{m=0}^{\infty}\frac{(-1)^m(2m+1)}{(1+iC_m)}\right|. \tag{4.8}$$

R is a function of acoustic radius, the dimensionless product of the fluid medium's wave number k and the radius a of the spherical scatterer:

$$ka = \left(\frac{\omega}{c}\right)a = \left(\frac{2\pi f}{c}\right)a. \tag{4.9}$$

4.2 Frequency-Domain Analysis

Anderson's expression for the reflectivity factor R has been implemented as a code in MATLAB (Program 4.1 in Appendix B), which can be used to generate frequency spectra for individual spherical scatterers immersed in fluid media. The input parameters for the MATLAB numerical computation include scatterer radius and the densities of and acoustic speeds in both the scatterer and surrounding medium. Although the convergence of the series in Equation 4.8 has not been explicitly examined, it is generally assumed that the range $0 \leq m \leq 50$ yields valid numerical results for reflectivity.

To verify this assumption and that the code accurately replicates the Anderson model, the graphs presented in Anderson's paper were reproduced using MATLAB. Two examples of these graphs are presented in Figures 4.1 and 4.2. Figure 4.1 shows the reflectivity R for direct backward scattering as a function of acoustic radius ka for various values of relative density g and relative acoustic speed h. It is evident that spheres with low values of g and h produce a backscatter exhibiting resonance behavior, while rigid spheres and those with higher g and h values yield smoother, moderate fluctuations in backscatter amplitude. In Figure 4.2, the reflectivity R for direct backward scattering is plotted as a function of both acoustic radius and relative acoustic speed. For this particular graph, the spherical scatterer and surrounding medium have the same density. As h increases, the direct backward scattering reveals increasing resonance behavior. Both Figure 4.1 and 4.2 match the graphs presented in Anderson's analysis.

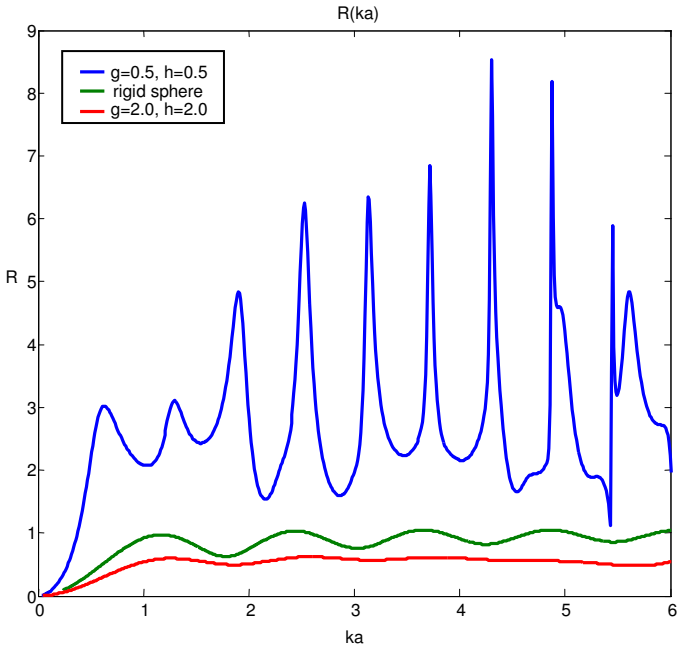

Figure 4.1 Graph of reflectivity *R* for direct backward scattering as a function of acoustic radius *ka* for various values of relative density *g* and relative velocity *h*.

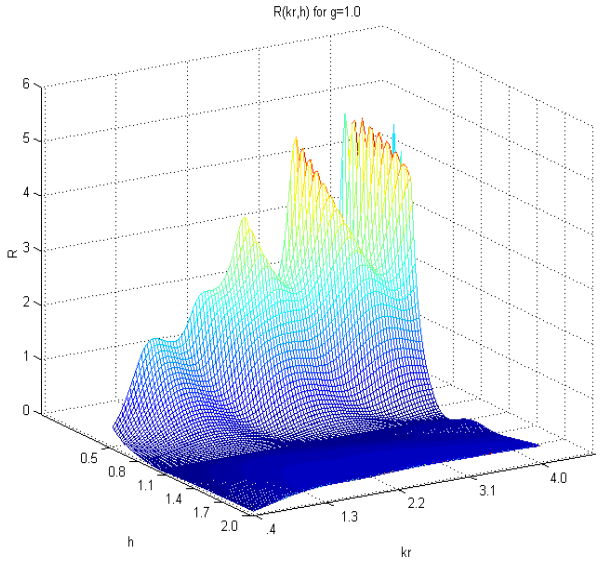

Figure 4.2 Graph of reflectivity *R* for direct backward scattering from a fluid sphere as a function of acoustic radius *ka* and relative acoustic speed *h* for a relative density *g* of 1.0.

In this particular study, the relevant range of acoustic radius in Equation 4.9 is ka = 0.08 – 4.8, where the wave number k depends on the frequency range 2 to 6 MHz and the scatterer radius a varies from 10 to 200 microns. To account for attenuation of ultrasonic waves in the scatterer and surrounding medium, a complex wave number is specified:

$$ka = \left[\frac{\omega}{c} + i\alpha\right]a = \left[\frac{2\pi f}{c} + i\alpha\right]a. \tag{4.10}$$

Here, α is the attenuation coefficient in blood expressed in Np/m. The conversion from dB/cm to Np/m is as follows:

$$\alpha(Np/m) = 11.513\alpha(dB/cm). \tag{4.11}$$

Estimated attenuation coefficients for relevant materials are presented in Table 4.1 [15-17].

Material	**Attenuation coefficient at 1 MHz (dB/cm)**	**Attenuation Coefficient at 1 MHz (Np/m)**
Air	≈ 0 dB/cm	≈ 0 Np/m
Water	0.0002 dB/cm	0.0023 Np/m
Blood	0.18 dB/cm	2.1 Np/m
Fat	0.5-1.8 dB/cm	5.8-20.7 Np/m

Table 4.1 The attenuation coefficients for various materials at 1 MHz [15-17]. Note that the attenuation coefficient used for air is approximately zero.

Generated using our MATLAB implementation of Anderson's model, Figure 4.3 illustrates the reflectivity as a function of acoustic radius for gas microemboli in blood. The color-coded plot indicates the *ka* range for a specified bubble of radius *a*. The black segment of this curve, for instance, represents a theoretical frequency spectrum of a 200-micron air bubble in blood. Note that for a given radius, the acoustic radius *ka* is a function of frequency.

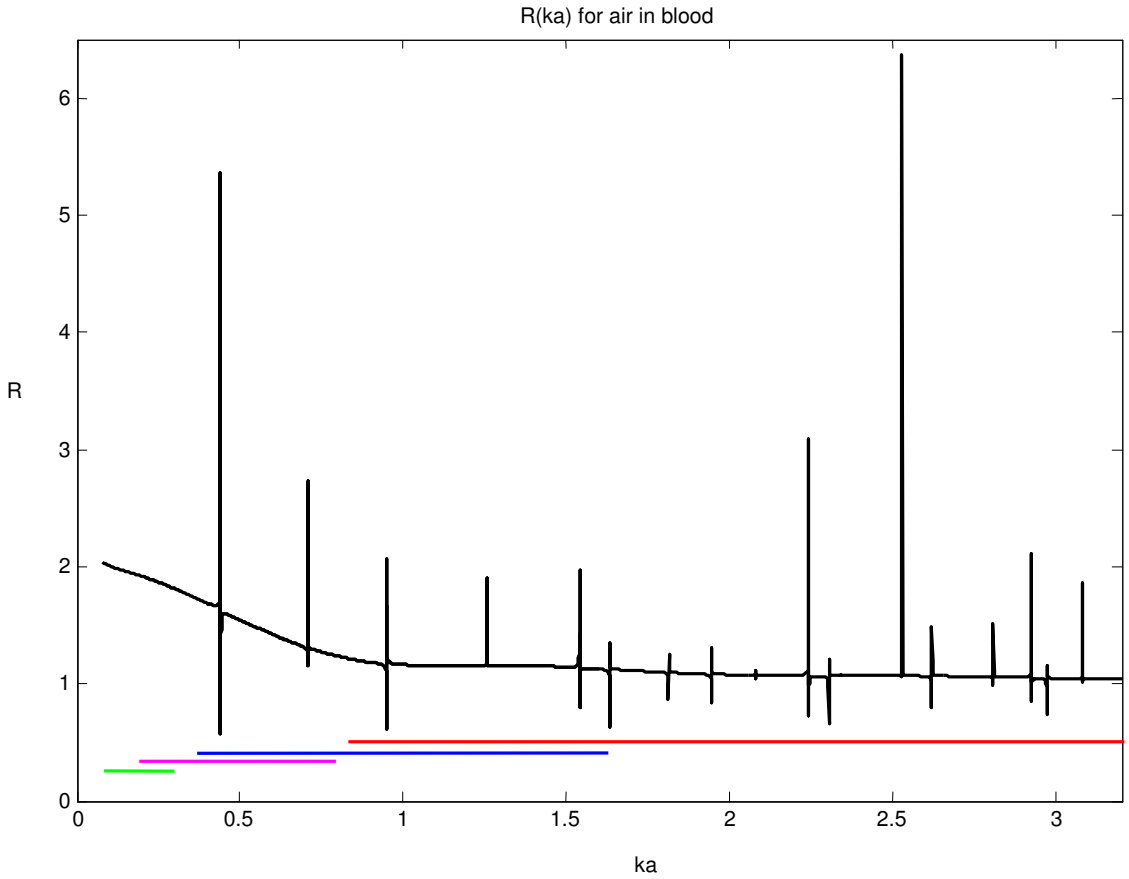

Figure 4.3 The reflectivity as a function of acoustic radius for air in blood. The colored lines beneath the curve indicate the range of acoustic radius for bubbles of varying diameter: 20μm (green), 50μm (blue), 100μm (magenta), and 200μm (red).

Likewise, Figure 4.4 shows the reflectivity of fat microemboli, and Figure 4.5 shows the reflectivity of clot-like emboli in blood. It is evident that the structures of frequency spectra for gas, fat, and clot-like emboli in blood differ significantly. While the backscatter from air exhibits a structure with sharp resonances, the backscatter plots for fat and clots resemble smoother, oscillatory curves. Figures 4.6 and 4.7 illustrate the reflectivity factor for air and fat as a function of both frequency and bubble size.

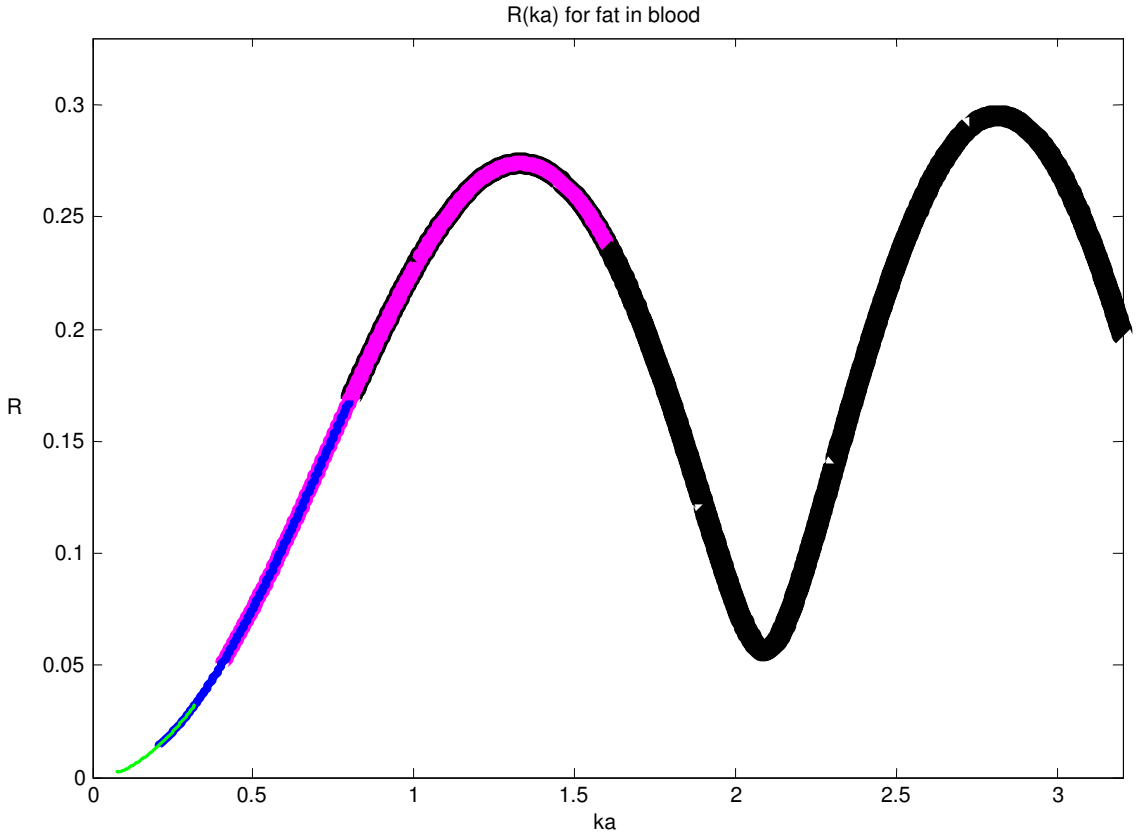

Figure 4.4 Reflectivity as a function of acoustic radius for fat in blood. The colored segments of the curve represent the range of acoustic radius for bubbles of varying diameter: 20μm (green), 50μm (blue), 100μm (magenta), and 200μm (black).

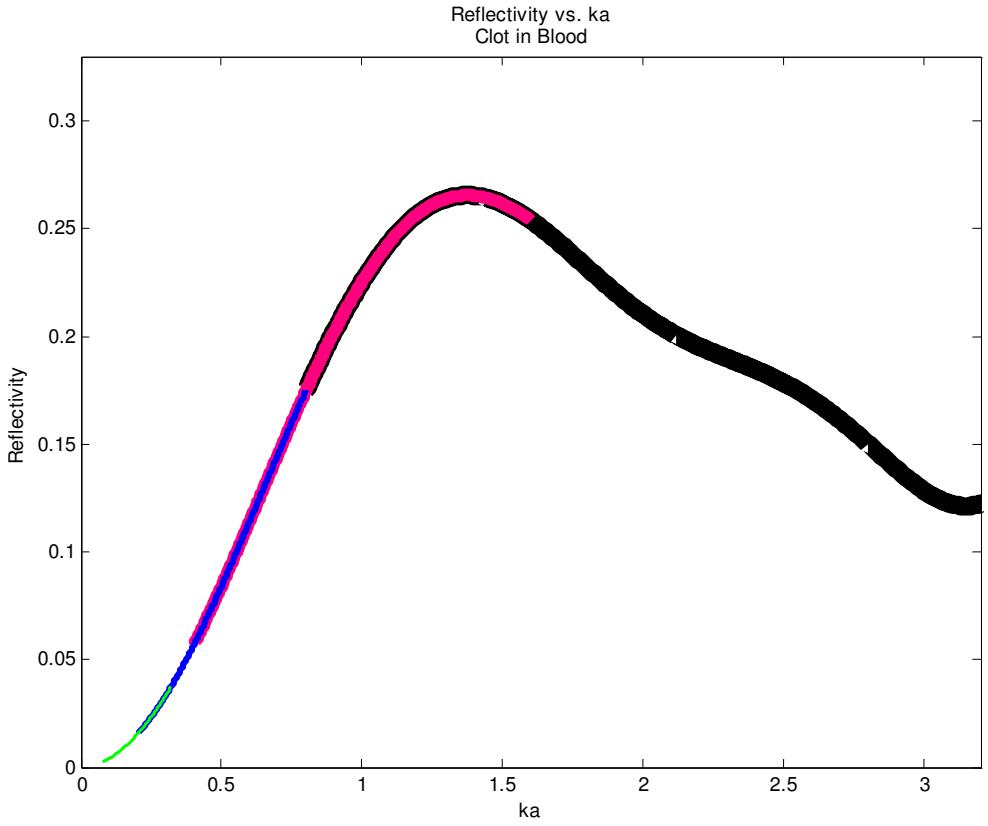

Figure 4.5 Reflectivity as a function of acoustic radius for clot in blood. The colored segments of the curve represent the range of acoustic radius for bubbles of varying diameter: 20µm (green), 50µm (blue), 100µm (magenta), and 200µm (black).

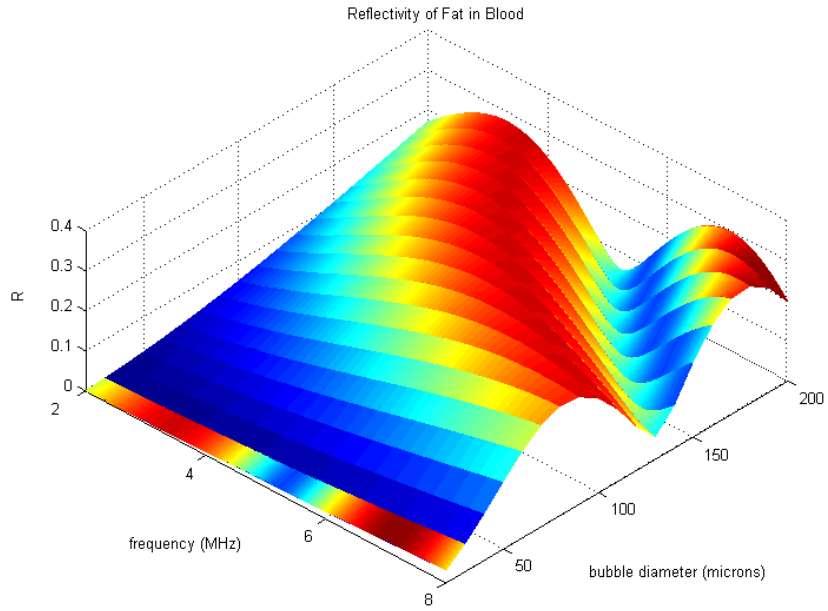

Figure 4.6 Reflectivity as a function of frequency and bubble diameter for fat in blood.

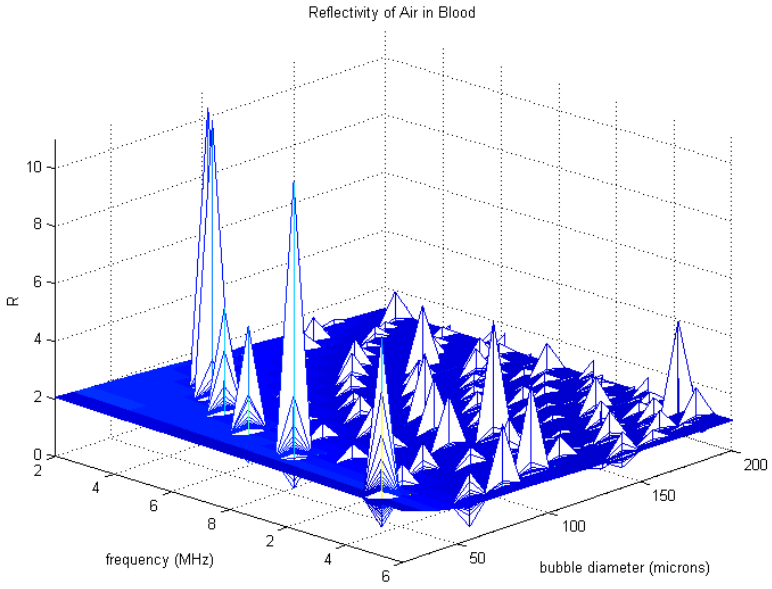

Figure 4.7 Reflectivity as a function of frequency and bubble diameter for air in blood.

The shape of the curve for gas emboli in Figure 4.3 resembles the theoretical backscatter of a vacuum bubble in fluid, as shown in Figure 4.8. The theoretical reflectivity of a spherical vacuum scatterer may be expressed as the limit of R as the relative density g approaches zero and can be considered the background backscatter for a soft acoustic sphere. The following limit of C_m in Equation 4.6 was used to generate the theoretical reflectivity curve in Figure 4.8:

$$\lim_{g \to 0} C_m = \frac{y_m(ka)}{j_m(ka)}. \tag{4.12}$$

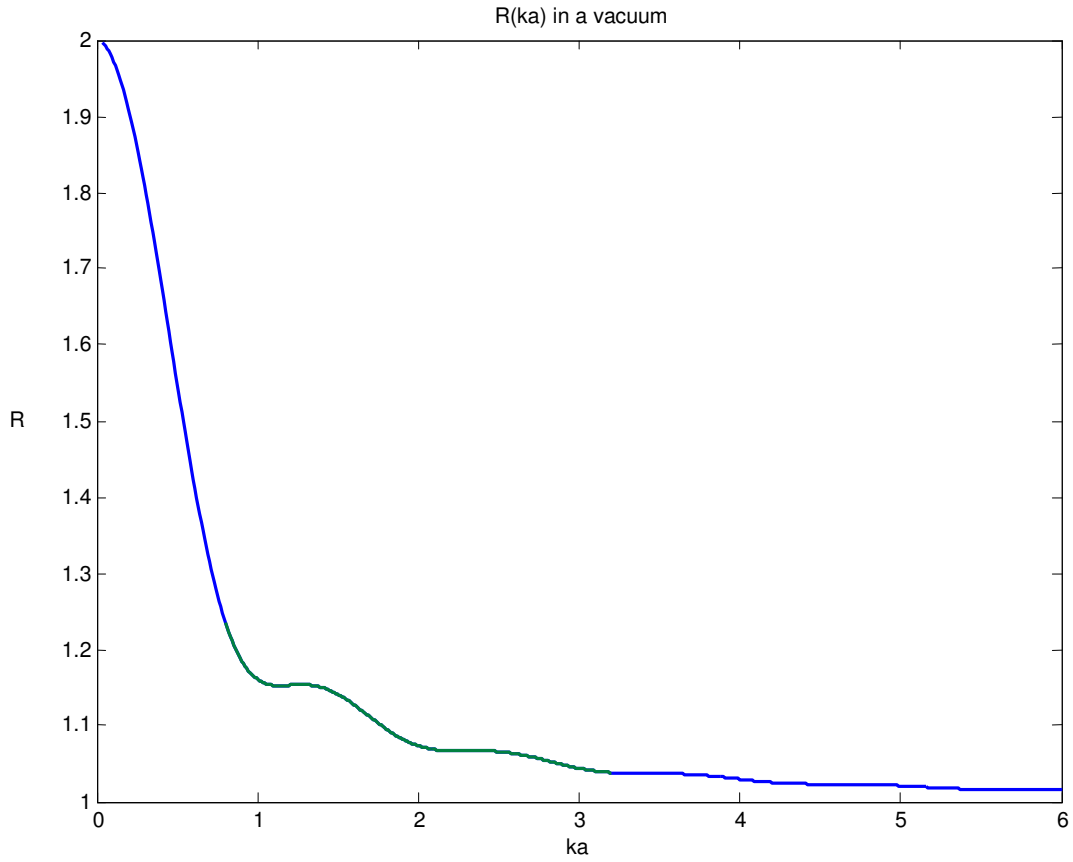

Figure 4.8. Theoretical backscatter for a vacuum bubble in fluid. This may be considered the background of an air bubble in water or blood. The green section of the curve is the portion significant for ultrasonic frequencies between 2 and 8 MHz and scatterer radii in the range of 10 to 100 μm. Note that as *ka* increases, the reflectivity approaches unity.

Considering Anderson's numerical examples and similar findings published by R.K. Johnson [14], the narrow resonances in the air embolus spectrum are most likely inherent in the analytical scattering solutions, rather than a result of MATLAB imprecision. When the background illustrated in Figure 4.8 is subtracted from the reflectivity curve, the resonances can be isolated as shown in Figure 4.9. A discussion of the relevance of these isolated resonances follows in Chapter 6.

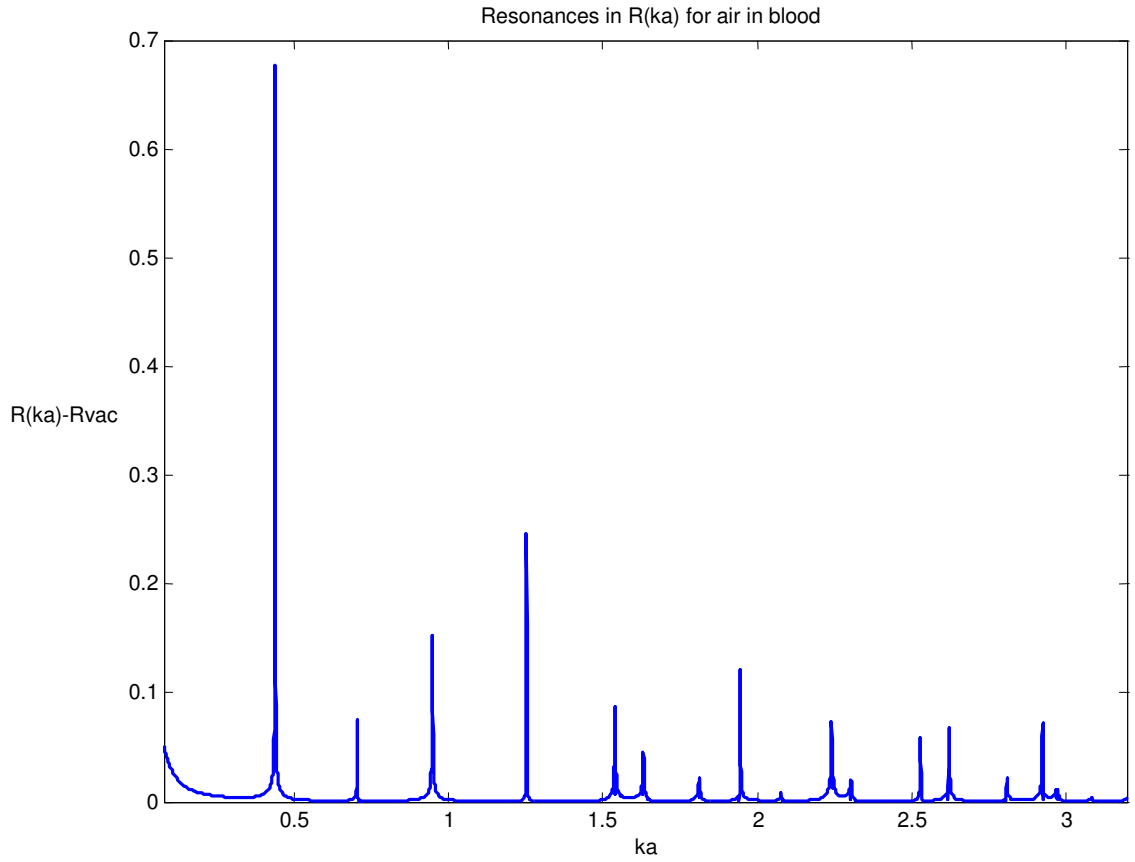

Figure 4.9 Isolated resonances for an air bubble of radius 100 μm in blood. This graph is obtained by subtracting the background (Figure 4.8) from the reflectivity curve for an air embolus in blood (Figure 4.3).

4.3 Testing of Material Parameters

To test the specific values of acoustic speed used to produce Figs. 4.3 - 4.5, we examined the effects of reasonable deviation in the acoustic speed parameter. The reflectivity was additionally plotted for various combinations of embolic and medium compositions presented in Table 4.2, which provides a list of the relevant materials' acoustic properties [14-17]. Table 4.2 additionally contains graphs of reflectivity plotted as a function of *ka*, similar to Figs. 4.3 - 4.5.

Embolus	Embolus Properties	Medium	Medium Properties	Average Acoustic Speeds	*R* (*ka*)
Fat	a = 100 μm ρ_f = 0.918 g/cm^3 c_f = 1430-1470 m/s	Water	ρ_w = 1.00 g/cm^3 c_w = 1510-1570 m/s	c_f = 1455 m/s c_w = 1510.6 m/s	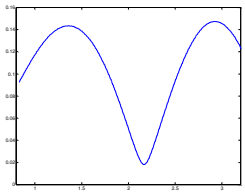
		Blood	ρ_b = 1.06 g/cm^3 c_b = 1540-1600 m/s	c_f = 1455 m/s c_b = 1570 m/s	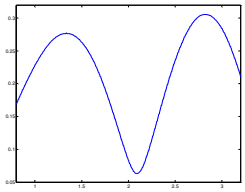
Castor Oil	a = 100 μm ρ_{oil} = 0.945 g/cm^3 c_{oil} = 1470-1530 m/s	Water	ρ_w = 1.00 g/cm^3 c_w = 1510-1570 m/s	c_{oil} = 1500 m/s c_w = 1510.6 m/s	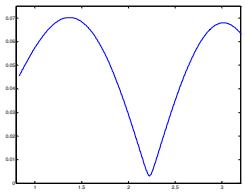
		Blood	ρ_b = 1.06 g/cm^3 c_b = 1540-1600 m/s	c_{oil} = 1500 m/s c_b = 1570 m/s	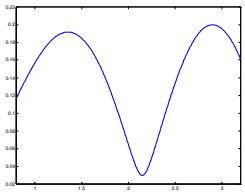
Air	a = 100 μm ρ_a = 0.0013 g/cm^3 c_a = 321-341 m/s	Water	ρ_w = 1.00 g/cm^3 c_w = 1510-1570 m/s	c_a = 331.45 m/s c_w = 1510.6 m/s	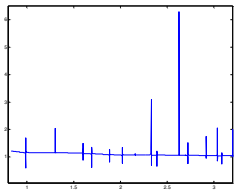
		Blood	ρ_b = 1.06 g/cm^3 c_b = 1540-1600 m/s	c_a = 331.45 m/s c_b = 1570 m/s	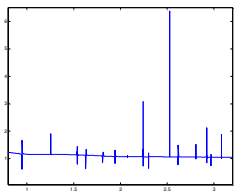

Table 4.2 The Matlab implementation was used to generate graphs illustrating the reflectivity of a spherical scatterer that resembles an embolus in an inviscid fluid medium. Here, the backscatter of bubbles of various compositions is plotted as a function of acoustic radius *ka*. Each embolus type is considered in fluid media of blood and water. The values *a*, ρ, and *c* designate the radius of the spherical scatterer, density, and acoustic speed, respectively.

Note that the backscatter of emboli in blood is very similar to that of the same emboli in water. It was found that when the acoustic speed changes for fat or castor oil emboli, the reflectivity curve retains the same general behavior, but deviates slightly in amplitude. Specifically, the reflectivity amplitude changes by a maximum factor of several hundredths for every 10-30m/s deviation in acoustic speed. Since this change is relatively minor, average acoustic speeds were selected for use in further calculations. The clot parameters used to generate Figure 4.5 were estimated using the acoustic properties of comparable soft solids [14-17].

To approximate the attenuation coefficient at frequencies greater than 2 MHz, a one-to-one linear relationship between frequency and the attenuation coefficient was implemented. Figure 4.10 shows the backscatter of a 200-micron fat embolus with various values of attenuation in the spherical scatterer. For physical attenuation values, the attenuated curve exhibits small deviation from the unattenuated curve. As expected for high, unphysical attenuation values, the curve deviates significantly from its unattenuated behavior. Figure 4.11 illustrates the backscatter of the same fat embolus for various values of attenuation in the medium surrounding the embolus. It is evident that the attenuation in the medium causes less deviation in the reflectivity curve than attenuation in the embolus.

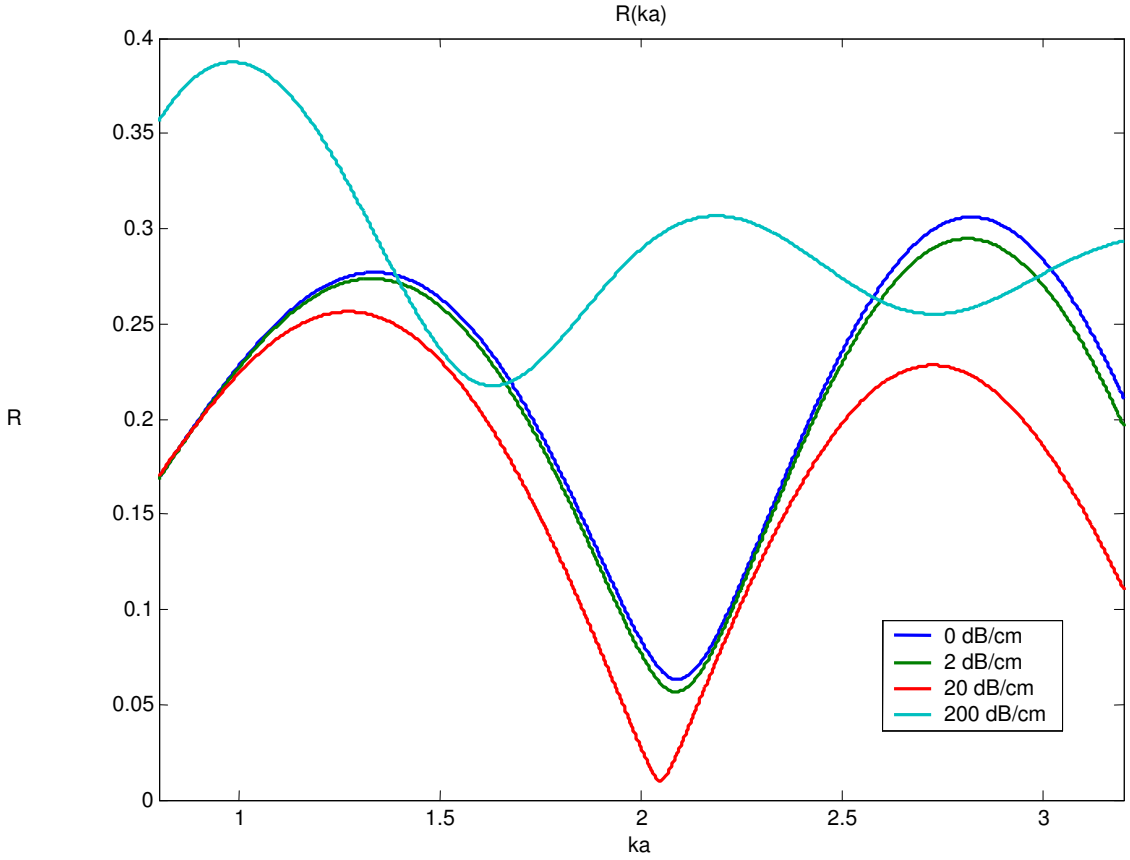

Figure 4.10 Backscatter from a 200μm fat embolus in blood for various values of scatterer attenuation. For each of these curves, the attenuation in the medium is zero. The legend on the lower right indicates the curves for various embolus attenuation coefficients at 1 MHz. The dark blue curve represents the reflectivity when there is no attenuation in the scatterer. The green curve shows the reflectivity with attenuation expected in fat. The red and light blue curves use unphysical attenuation coefficients for fat at 1 MHz.

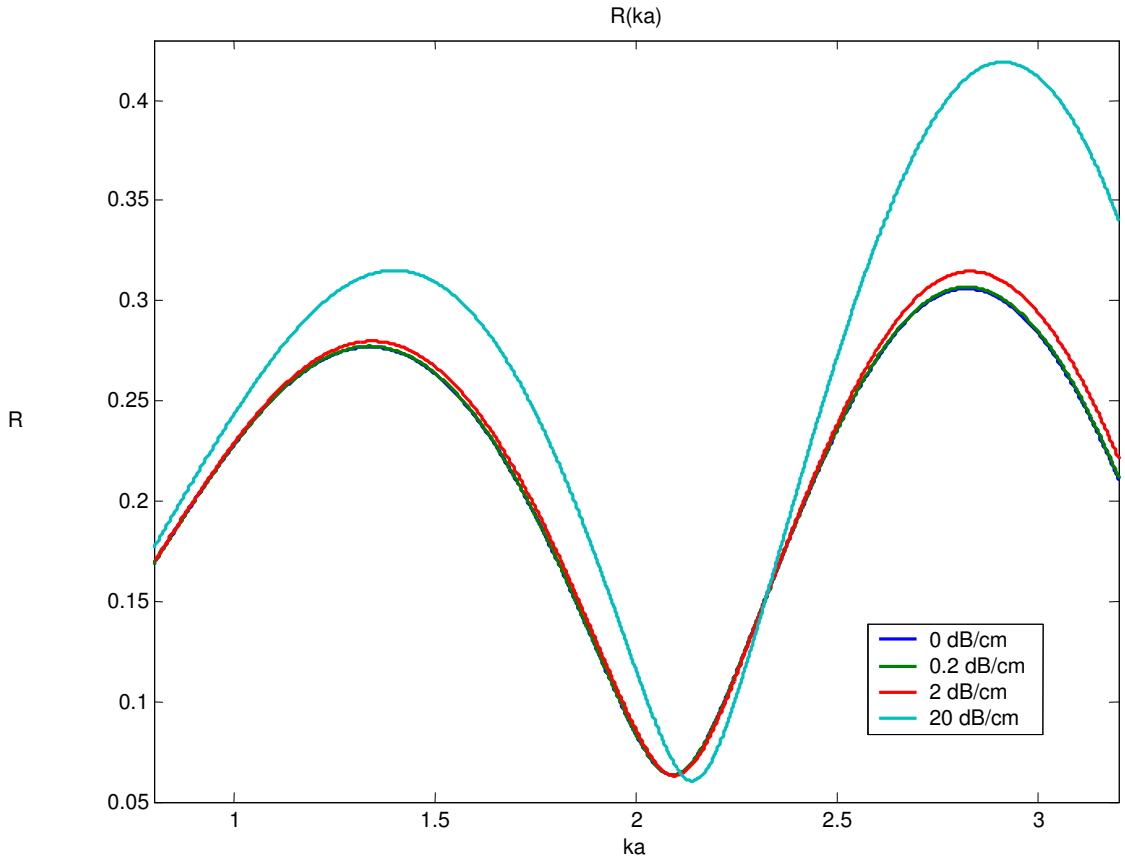

Figure 4.11 Backscatter from a 200μm fat embolus in blood for various values of attenuation in the medium. For each of these curves, the attenuation in the embolus is zero. The dark blue curve represents the reflectivity when there is no attenuation in the medium. The green curve, which is barely distinguishable, shows the reflectivity with the attenuation expected in blood. The red and light blue curves are for unphysical attenuation coefficients for blood at 1 MHz.

In the case of a gas embolus in blood, the attenuation coefficient appears to have less influence on the reflectivity curve. In Figure 4.12, the unattenuated curve is shown in blue and the attenuated curve is shown in green. Clearly it is difficult to distinguish the two curves, which differ by only two thousandths on the vertical axis. For these calculations, the attenuation coefficient for air is approximately zero. This approximation is appropriate since the attenuation coefficient for air is less than that of water, the former being on the order of 10^{-3} Np/m. When multiplied by a radius on the micron scale, the complex component of the acoustic radius for air microemboli becomes negligibly small.

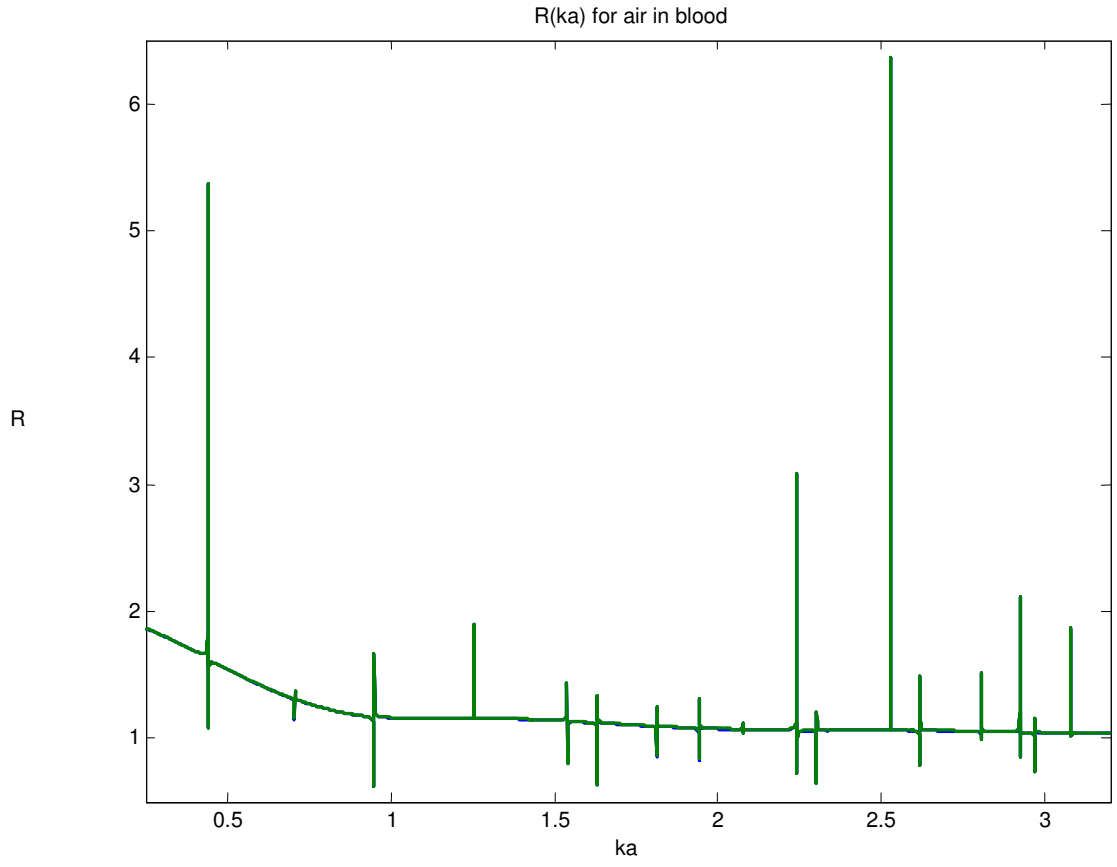

Figure 4.12 The backscatter of a 200-micron air embolus in blood. The dark blue curve shows the reflectivity without attenuation in the embolus or medium. The superimposed green curve accounts for attenuation in both the embolus and medium.

Had our experimental setup been *in vivo*, it is likely that attenuation of propagating ultrasound pulses would have greater effect on reflectivity, as the waves would need to propagate through layers of skin and tissue before impinging upon and scattering from emboli in the bloodstream. Since our analysis focuses on scattering from fluid in extracorporeal circuits, these sources of significant dissipation effects need not be considered.

4.4 Scattering Effects of a Thin Layer Surrounding the Embolus

The MATLAB implementation of Anderson's scattering solutions has also been modified to characterize the backscatter from a fluid sphere of radius a that is surrounded by a thin layer of material with thickness b-a, as shown in Figure 4.13. The four unknown scattering coefficients for this problem were determined by applying the appropriate boundary conditions: the pressure and normal velocity component must be continuous at each interface of the spherical scatterer. The input parameters for this code (Program 4.2 in Appendix B) include the lengths of radii a and b, and the material properties of the embolus, the thin layer, and the surrounding medium. To verify the mathematical foundations for this code, the limit as a approaches b was taken, and the result matched Anderson's theoretical expectations.

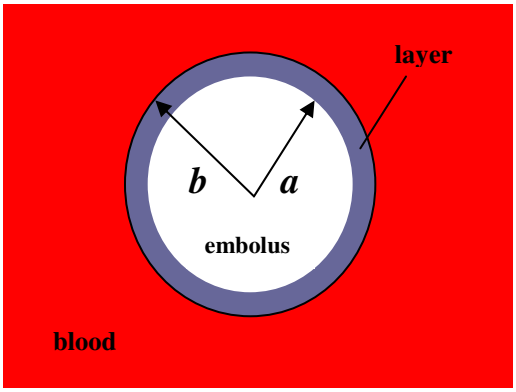

Figure 4.13 Diagram of an embolus surrounded by a thin shell of material.

The MATLAB code was similarly verified by evaluating ultrasonic backscatter when the material properties of the embolus and surrounding layer were identical. For example, it was demonstrated that the backscatter from a 200μm fat embolus matched that of 200μm embolus for which a = 90μm, b = 100μm, and both the embolus and surrounding shell had the acoustic properties of fat. Likewise, the code was tested for a 200μm air embolus, resulting in the same confirmation. In addition, the MATLAB implementation was used to examine the backscatter from a hypothetical 90μm air embolus surrounded by a 10μm layer of fatty material. The resulting curve, Figure 4.14, is similar to that for an air embolus without a surrounding layer; however, the new curve exhibits a vertical shift and resonance deviations.

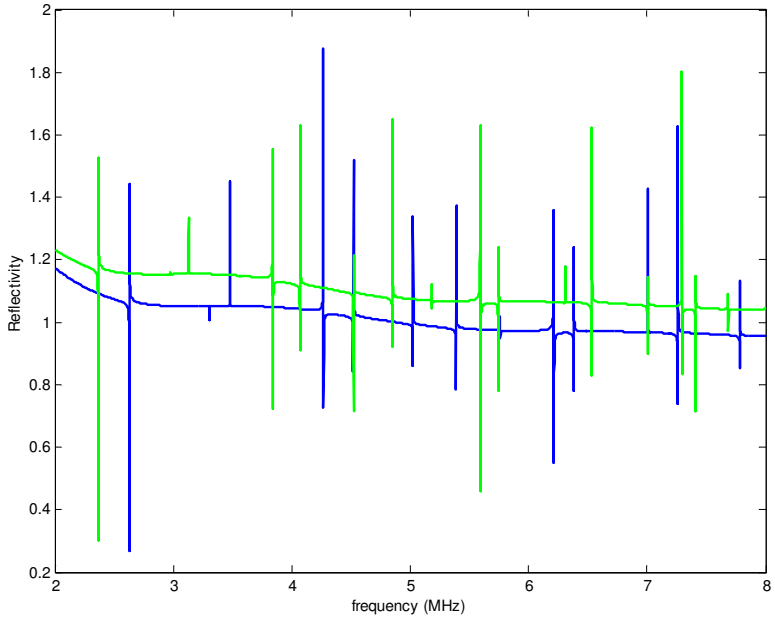

Figure 4.14 The blue curve is the reflectivity of a 200-micron air bubble in blood. The green curve is the reflectivity of an air embolus surrounded by a layer of fatty material, where a = 90 microns and b = 100 microns.

The modified code was used to generate mesh plots and contour plots of reflectivity as a function of transducer frequency and acoustic speed in the shell for shell densities of 500 kg/m^3, 1000 kg/m^3, and 2000 kg/m^3. In each case, the embolus had a radius of 100μ with either a 10μ-

or 30μ-shell. The transducer frequency range was 2-8MHz, and the acoustic speed in the shell ranged from 300-2300m/s. Plots were generated and interpreted for both air and fat emboli.

For air emboli with a 10μ-shell, the reflectivity curves closely resemble the theoretical backscatter from a vacuum bubble. Several peaks in reflectivity occur at higher frequencies between 5-8MHz. For air emboli with a 30μ-shell, the reflectivity again resembles that of a vacuum bubble but with extensive resonance behavior at low acoustic speeds (less than 800m/s). For greater shell densities, these resonances occur at decreasing acoustic speeds in the shell. In other words, the resonances occur linearly as a function of frequency and acoustic speed, and the linear behavior exhibits a decrease in slope as shell density increases. This characterization of linear behavior is qualitative, rather than rigorously quantitative, in nature.

For fat emboli with a 10μ-shell, the reflectivity curves resemble those for fat emboli without a surrounding layer. For lower shell densities, the backscatter exhibits increasingly exaggerated curvature for acoustic speeds of 1000m/s and lower. Similar to the air embolus backscatter, the fat embolus backscatter features linearity at low acoustic speeds. The slope of this linear behavior decreases as shell density increases. Fat emboli with 30μ-shells feature similar behavior compared to those with thinner shells. As the shell thickness increases, however, the curvature in the embolus backscatter becomes increasingly suppressed.

For clinical relevance, the material properties of relevant emboli and their surrounding shells must be specified.

Chapter 5: Time-Domain Analysis and Simulation Comparison

5.1 Analytical Time-Domain Analysis

The usefulness of the frequency-domain analysis lies in its potential as a tool to interpret experimental data collected in time domain. First we verify that time-domain reflections obtained using our model can be used to effectively model experimental ultrasonic interactions.

Consider the frequency spectrum of an air bubble in blood, shown in Figure 4.3. In MATLAB we numerically evaluate the real component of its inverse fast Fourier transform, resulting in a time-domain curve. Next we convolve this waveform with a sample excitation pulse shown in Figure 5.1. This pulse is a 3-cycle 3.9-MHz sine wave, sampled at 48 MHz (the digitization rate of the EDAC device) and filtered with a Hanning window.

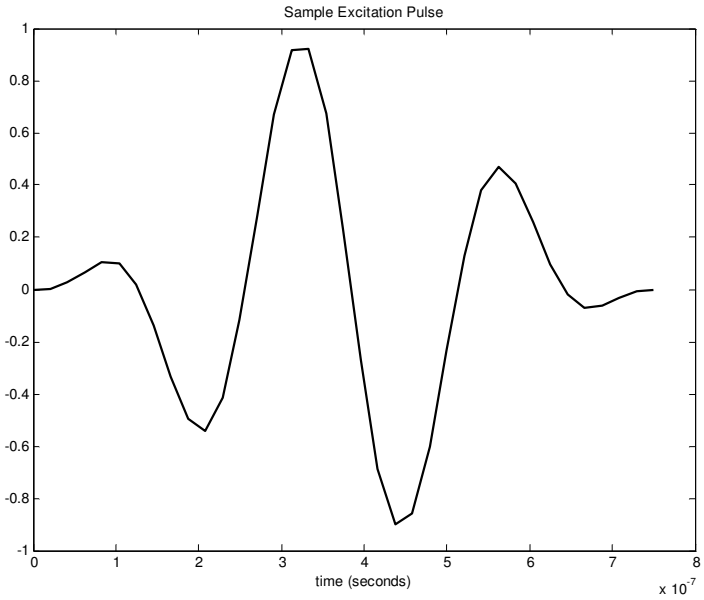

Figure 5.1 Sample excitation pulse emitted by transducer.

If such a waveform were scattered from a 200-micron air bubble in blood, our theoretical model indicates that we would receive the form of the time-domain reflection presented in Figure 5.2, which we obtain by convolving the IFFT of the bubble's frequency spectrum with the specified

excitation pulse. Theoretically, the convolution of these time-domain waveforms is equivalent to multiplying their frequency spectra and taking the IFFT of the resulting spectrum.

Figure 5.2 Theoretical time-domain waveform reflected from an air bubble in blood.

5.2 Comparison of Analytical and FDTD Approaches

The following characteristics of the Anderson-based model should be highlighted: First, the analysis is inherently in frequency domain. It provides exact, steady-state analytical solutions for direct backscatter from fluid spheres as functions of frequency. Second, the excitation source in this model is an infinite plane wave, as opposed to a finite source in the experimental setting. Third, the definition of the reflectivity factor *R* provides for a scattered waveform with normalized pressure amplitude. Considering these factors, it is useful to compare our model to one that is implemented in time domain, accounts for the geometry of the finite excitation source, and provides measurements of the pressure amplitude of the scattered waveforms.

To thus test the results of our analytical model, we utilize a time-domain MATLAB simulation developed by K.E. Rudd [18]. This simulation is a two-dimensional scattering model based on the cylindrical acoustic finite integration technique (CAFIT), which accounts for the cylindrical geometry of the piezoelectric excitation source. The CAFIT approach establishes a discrete scheme for numerically determining wave motion in the two coordinates z and r, assuming axisymmetric wave propagation. It begins with dimensionless linear equations of continuity and motion and performs an integration of these differential equations over controlled areas in the r-z plane. The controlled areas compose a staggered grid, leading to better accuracy than alternate numerical procedures [18-19]. The input parameters of Rudd's simulation (Program 4.3 in Appendix B) include the acoustic properties of the spherical scatterer and its surrounding medium, transducer specifications, excitation pulse characteristics, and grid-space sizing.

Several frames from a sample CAFIT simulation are illustrated in Figure 5.3. Note that the transducer face is 0.5 cm in radius and situated 1 cm from the 300-micron air bubble. (Here we use a larger bubble size for illustrative purposes.) Figure 5.4 shows a resulting A-line, representing the general form of time-domain reflections received from an air microbubble in blood. The first waveform in the A-line is the excitation pulse, while the following waveform is a secondary incident pulse produced by the constructive interference of edge waves, apparent in the second frame of Figure 5.3. To form the incident plane wave, individual spherical waves are emitted from each point on the transducer face. While most of the spherical waves interfere to form the incident plane wave, several spherical waves remain at the edges. As the plane wave propagates along the z-axis, these edge waves interfere to produce the secondary incident pulse.

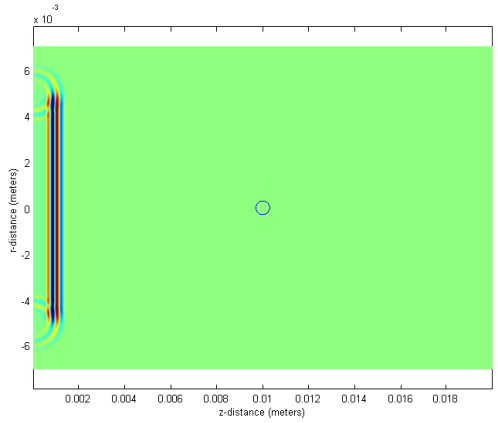

Frame 1

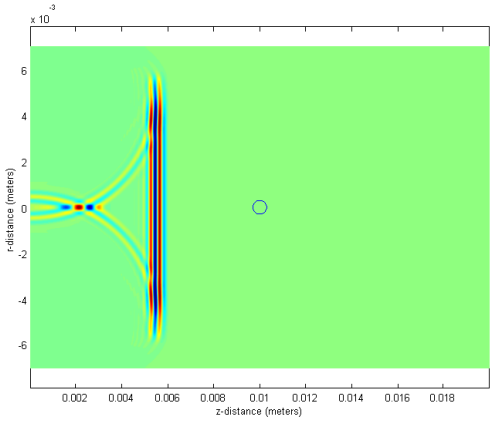

Frame 2

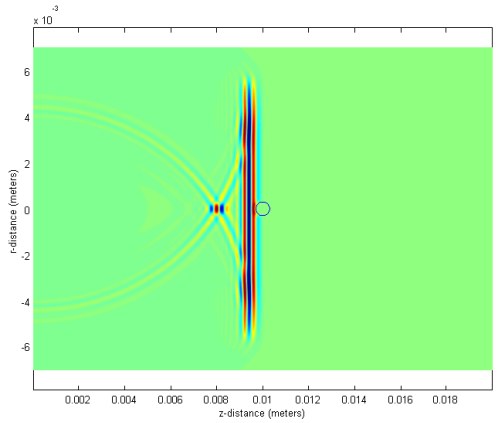

Frame 3

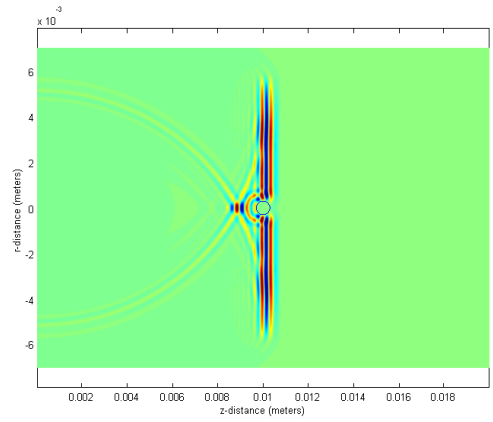

Frame 4

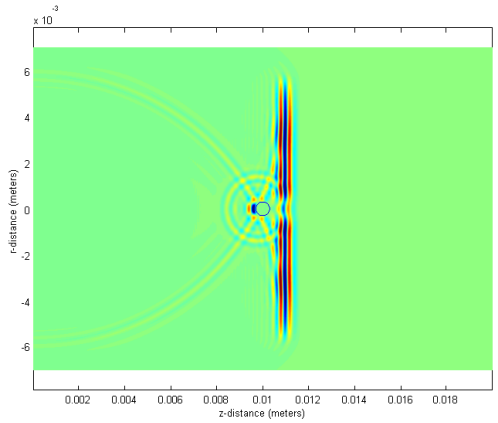

Frame 5

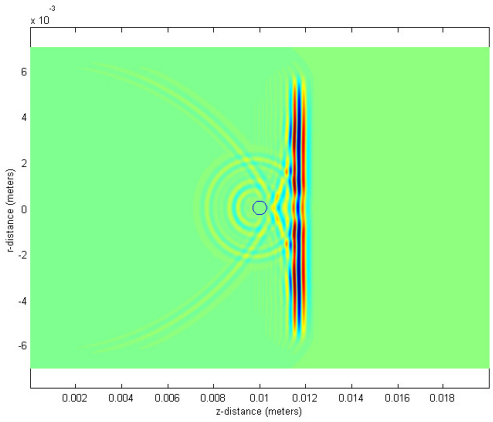

Frame 6

Figure 5.3 Frames from the CAFIT simulation, illustrating ultrasound scattering from air in blood.

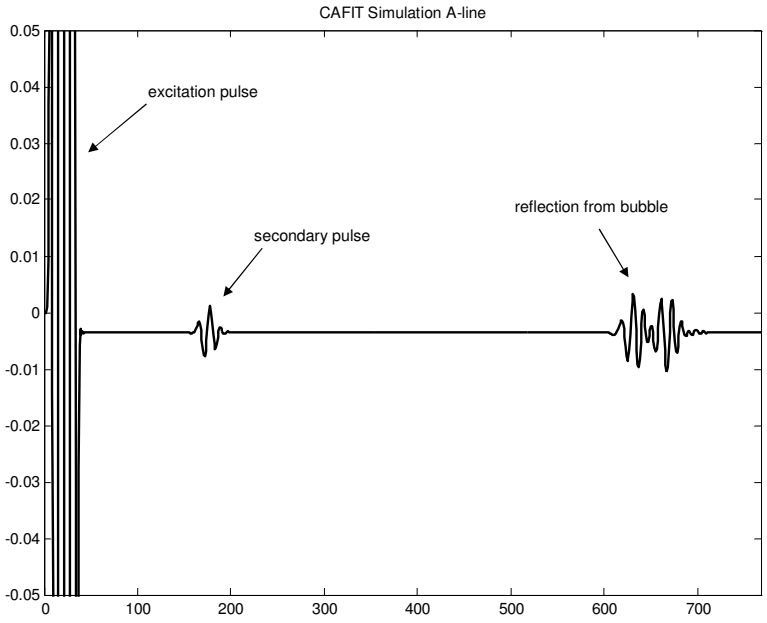

Figure 5.4 The A-line produced by the CAFIT simulation for a 300μm air bubble in blood.

The secondary pulse adds complexity to the ultrasound-bubble interaction. When the primary incident pulse scatters from the air bubble, it interferes with the secondary pulse before returning to the transducer. Then the modified secondary pulse, a convolution of the initial secondary pulse and scattered waveform, is reflected from the scatterer. The total received reflection is then a combination of 1) the reflection from the incident pulse convolved with the initial secondary pulse and 2) the reflection of the modified secondary pulse from the scatterer. The similarity of the CAFIT waveform and a patchwork produced using our analytical time-domain analysis is illustrated in Figure 5.5.

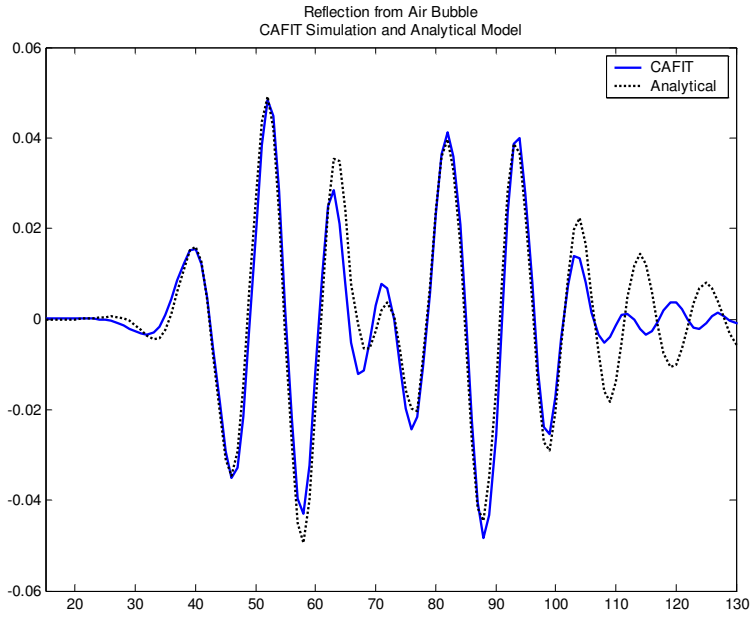

Figure 5.5 Time-domain reflection from air in blood. The CAFIT curve is shown in blue, and the analytical comparison is presented in black.

The secondary pulse has a seemingly significant impact on scattering, but the effects of this pulse are exaggerated by simplifying assumptions of the computational grid. While secondary pulses of this nature are common in real transducers, they are often attenuated through proper damping. Additionally, in the EDAC device, the ultrasound beam must pass through a transmission window that provides further damping of the signal. The secondary pulse, at 40 dB below the primary pulse, is therefore attenuated in real systems to below the background noise levels. By considering and better understanding the effect of edge waves on backscatter, however, we verify the consistency of the CAFIT simulation with a time-domain analysis of our analytical model.

Chapter 6: Sizing Gaseous Microemboli

6.1 Theoretical and Experimental Verification of Gaseous Embolus Sizing

The CAFIT simulation can be used in conjunction with the Anderson-based analytical model to validate a microbubble sizing scheme. Consider the reflectivity curve of an air bubble in blood, presented in Figure 4.3. Due to the 48-MHz sampling rate of the EDAC device, it is unlikely that the sharp resonances in this plot will be discernable in experimental data. Without this sampling rate limitation, the resonance features would likely provide a very accurate means of sizing air emboli. By considering the theoretical backscatter from a vacuum cavity in blood, we can observe the same reflectivity curve in Figure 4.3 without the resonances. The function $y(ka) = 0.25/ka + 0.96$, shown in Figure 6.1, provides a good approximation of this resonance-free curve. In our approximation of R, we assume the wave number k is constant despite some variation in bandwidth frequency.

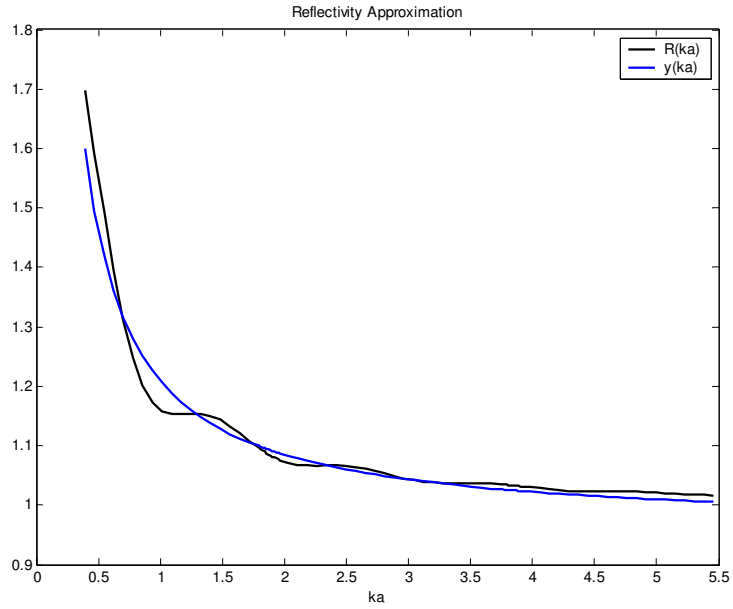

Figure 6.1 The theoretical backscatter from a vacuum cavity in blood, shown in black, is equivalent to the resonance-free reflectivity of air in blood. The function $y(ka)$, shown in blue, is the approximation of this curve.

Since Anderson defines the reflectivity as the ratio of the pressure amplitude of the scattered wave p to the geometric normalizing factor p_{geom}, we multiply R by p_{geom} to obtain the amplitude of the scattered wave:

$$R * \left| p_{geom} \right| = \frac{\left| p \right|}{\left| p_{geom} \right|} * \left| p_{geom} \right| = \left| p \right|. \tag{6.1}$$

Here we assume that the pressure amplitude of the incident wave is unity, which is consistent with the incident wave specified in the CAFIT simulation. Plotting the relative pressure amplitude as a function of bubble diameter, we observe a linear relationship between signal amplitude and bubble size as illustrated in Figure 6.2. Considering the approximation $R \sim y(ka)$, the linear proportionality between amplitude and diameter is expected: When y is multiplied by $p_{geom} = a/2r$, the result is a linear function of bubble diameter $2a$ with a slope equal to 24m^{-1}.

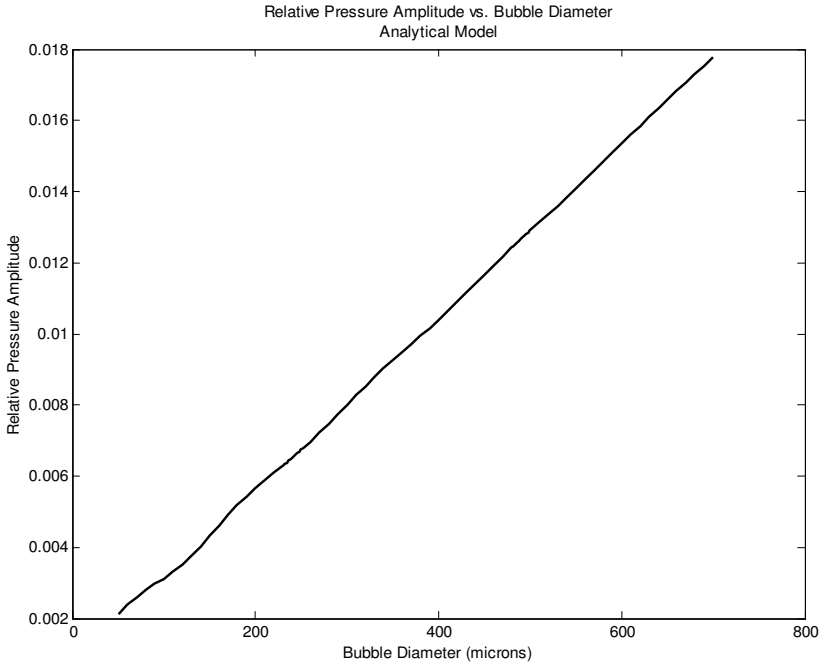

Figure 6.2 Relative pressure amplitude $|p|$ of the scattered wave plotted as a function of bubble diameter, according to Anderson's analytical model.

To verify our analysis, Rudd's CAFIT simulation was run for scatterers with diameters in the range of 50-700 microns at 5-micron increments. In these simulations we used the same input waveform and parameters specified in Chapter 5. Figure 6.3 illustrates the results of the simulations, indicating an overall linear relationship between signal amplitude and bubble diameter. Here, the signal amplitude is represented by the maximum of the Hilbert transform envelope of the reflection. (The Hilbert transform was applied to the time-domain waveform to create an envelope of the waveform, a representation of the amplitude modulation on the carrier wave frequency.) The slope of the best-fit line of these data points is $19m^{-1}$, compared to the $24m^{-1}$ slope of the analytical line.

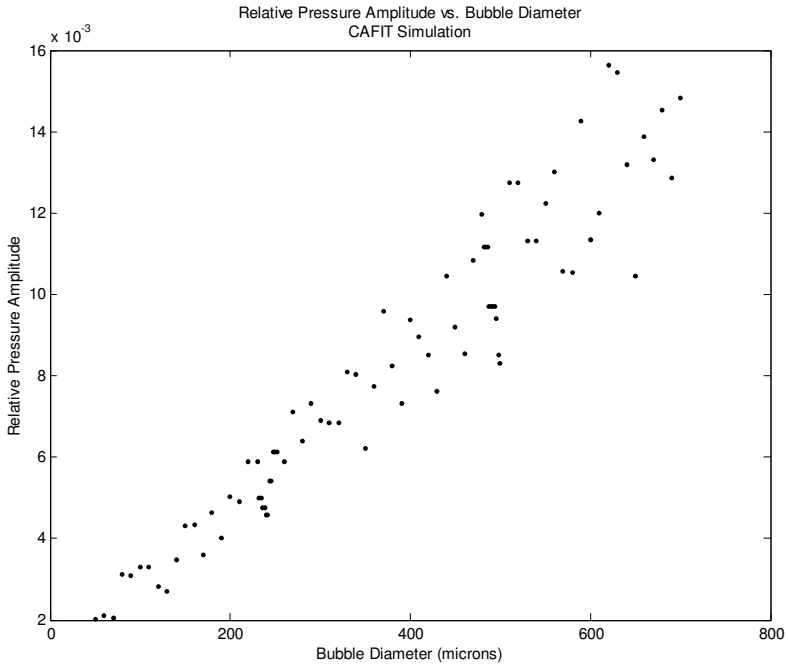

Figure 6.3 CAFIT simulation results. The relative pressure amplitude of the scattered wave as a function of bubble diameter.

Figure 6.4 shows the CAFIT results and best-fit line for the theoretical analysis. The plot suggests that the CAFIT results form a region, or beam, of amplitudes situated just beneath the theoretical curve. To account for the slope discrepancy, we first verified that the slope of the

analytical line did not change significantly with reasonable deviations in the wave number *k* and attenuation values in blood. Next we ran several CAFIT simulations with a sampling rate of 200 MHz, which resulted in greater amplitudes than previously obtained with the 48-MHz sampling rate. Considering the slight jaggedness of the CAFIT reflections at the 48-MHz sampling rate, our results suggest that the low sampling rate may contribute to slightly decreased amplitude measurements, thus reducing the slope in the plots of signal amplitude versus bubble diameter.

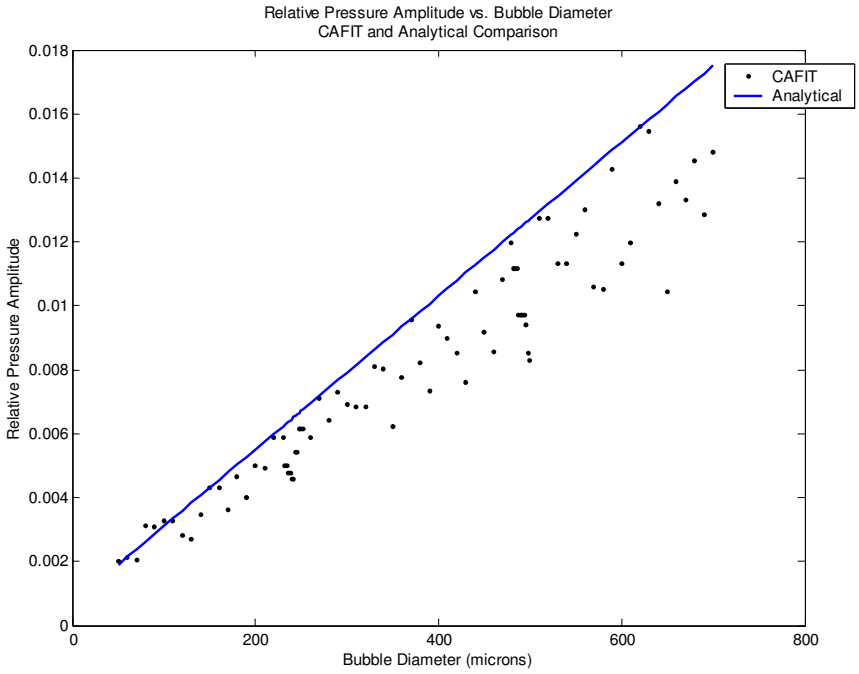

Figure 6.4 Relative pressure amplitude as a function of bubble diameter. The CAFIT simulation results are shown in black and the best-fit line of the theoretical analysis is shown in blue.

Experimental sizing tests were performed in which microscopic images of air bubbles injected into a closed loop test circuit were compared against EDAC derived ultrasound signal amplitudes. A linear regression between the EDAC echo amplitudes and the optical sizes was performed, the results of which are shown in Figure 6.5. For the triangular points, the diameter was measured using the CCD camera, and for the square points the diameter was measured using the USB microscope. The strong linear correlation between the values ($R^2 = 0.96$) is consistent

with the prediction of a linear relationship indicated by the analytic model and computer simulation.

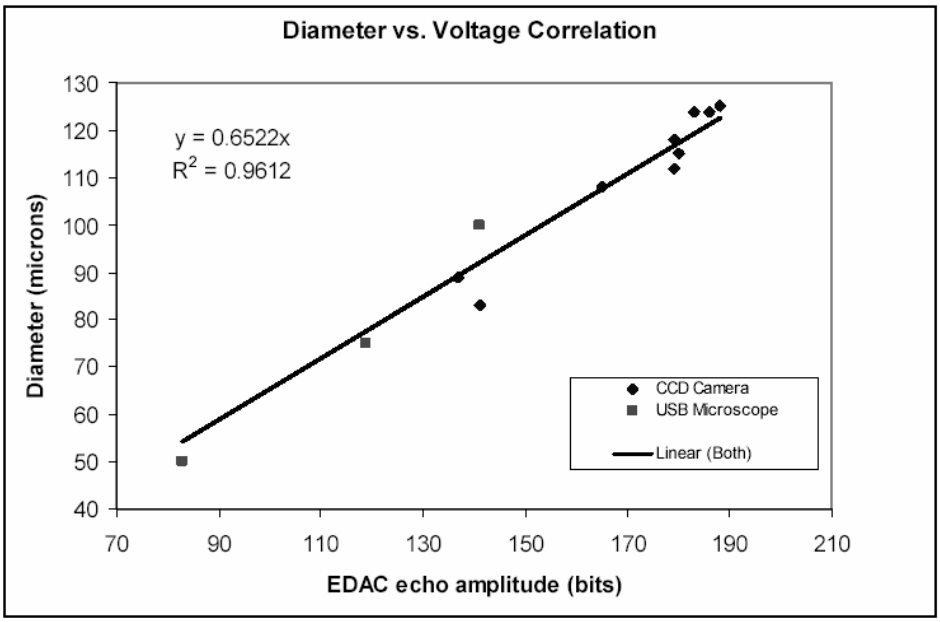

Figure 6.5 Experimental sizing tests were performed in which microscopic images of air bubbles injected into a closed loop test circuit were compared against EDAC derived ultrasound signal amplitudes. A linear regression between the EDAC echo amplitudes and the optical sizes was performed.

6.2 Phase Analysis

The scattered waveforms generated using the CAFIT simulation, similar to Figure 5.2, were analyzed to determine a potential relationship between phase and bubble diameter. Several of the waveforms scattered from air bubbles of varying size are presented in Figure 6.6. The time of the reception of the reflected waveform's first peak was determined for bubbles ranging 60 to 400 microns in diameter. Since the simulation situated the bubbles concentrically at a fixed distance from the transducer, the incident and reflected waveforms traveled farther for smaller bubbles. The extra time traveled by waves to and from bubbles smaller than 400 microns was subtracted from the time that the reflection was received. Once this concentric configuration was

accounted for, the time delays of the reflections relative to the 60-micron waveform were calculated. These time delays were then multiplied by $2\pi f$ to determine the phase shift of each waveform. The phase shift was plotted as a function of bubble diameter, shown in the Figure 6.7.

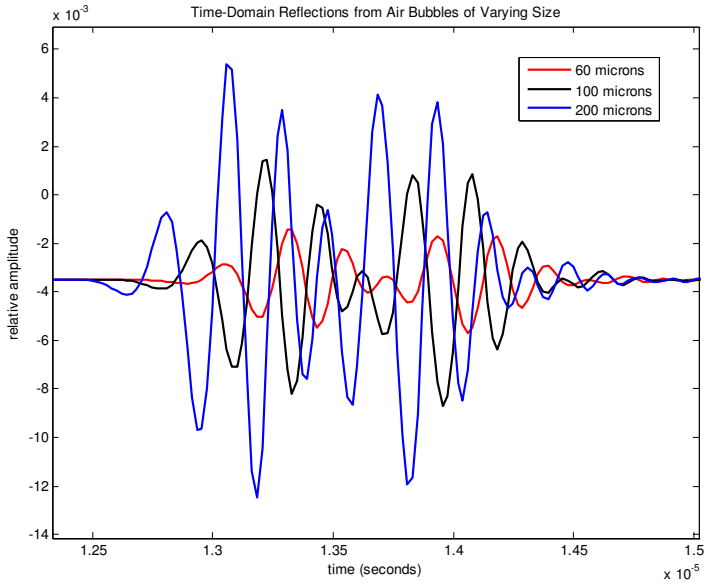

Figure 6.6 Several time-domain reflections from air bubbles of varying size. These curves were generated using the CAFIT simulation with the incident pulse presented in Figure 11.

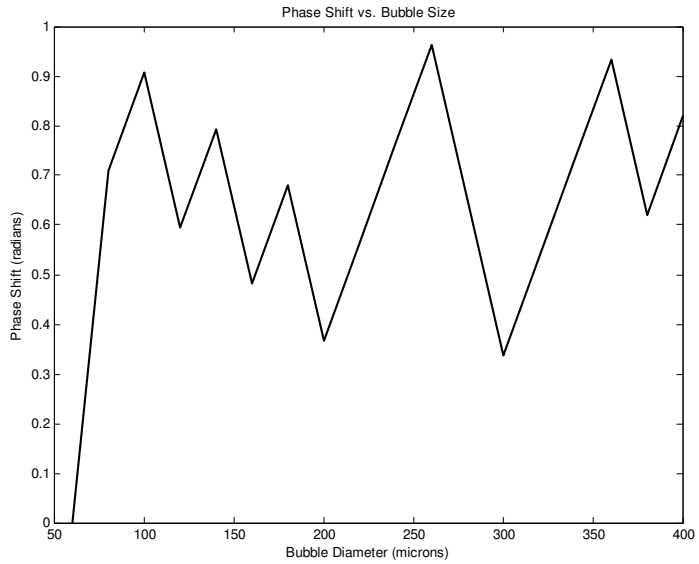

Figure 6.7 Phase shift as a function of bubble diameter using the incident pulse in Figure 11.

The CAFIT simulations were additionally run using a narrow incident pulse illustrated in Figure 6.8. The results of the phase analysis are shown in Figure 6.9, revealing no significant relationship between phase shift and air bubble diameter. This analysis suggests that the use of a transducer with narrower bandwidth would not likely improve embolus sizing based on phase.

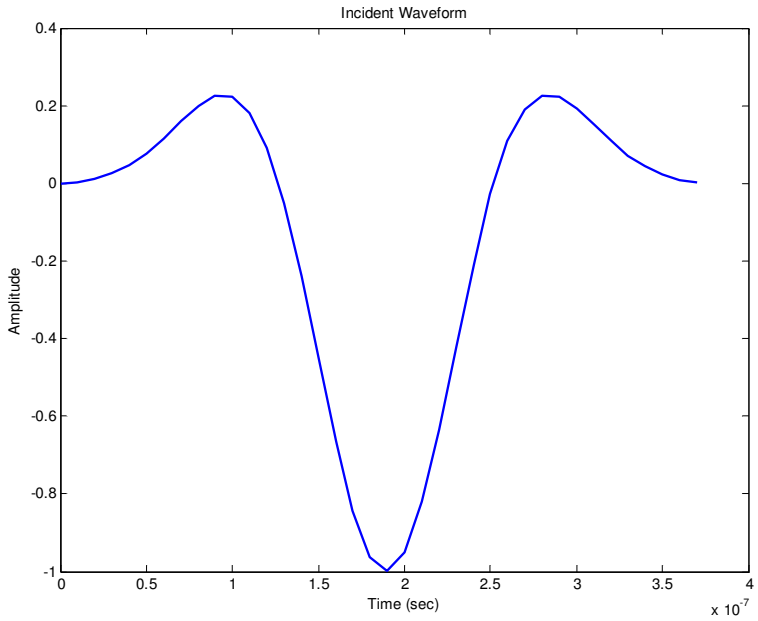

Figure 6.8 Narrow pulse used as the excitation pulse in the second part of the phase shift analysis.

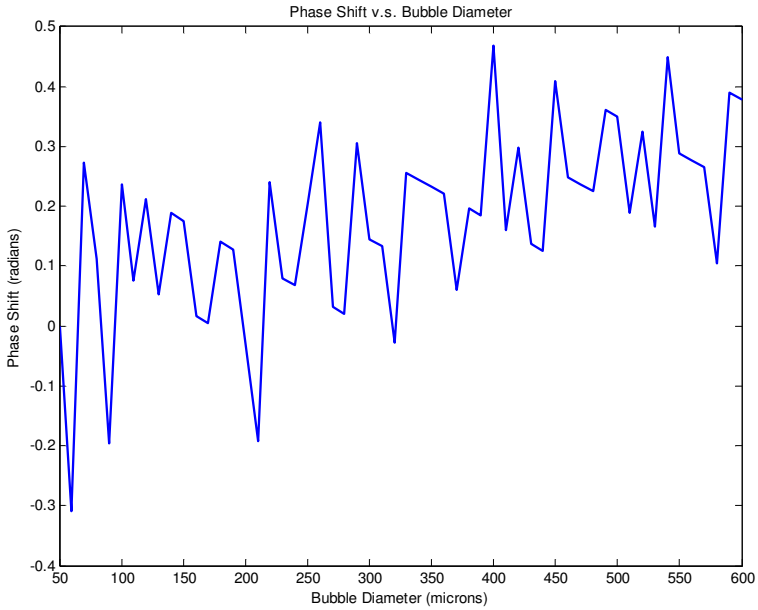

Figure 6.9 Phase shift as a function of bubble diameter with the incident pulse shown in Figure 23.

Chapter 7: Viscous-Fluid Model Analysis

As shown in Figs. 4.3 and 4.4, the smooth, oscillatory behavior of the lipid and clot-like emboli reflectivity curves is notably different from the reflectivity curve for air emboli. To consider the lipid case in further detail, we use an extension of the Anderson model that explores the extinction of sound by spherical scatterers in a viscous fluid [20]. Viscosity complicates the analysis since the fluid media can support both shear and compressional wave modes, both of which must be accounted for in boundary conditions at the scatterer's surface.

In Hinders' extension [20] of Anderson's analysis, the fluid medium within the spherical scatterer is assigned subscript 1 and the fluid medium in which the scatterer is embedded is assigned subscript 2. The center of the scatterer is again situated at the origin of the spherical coordinate system. Scattering solutions are investigated with the method of Herzfeld, but no restriction is placed on scatterer size. The equation of motion for harmonic time variation $e^{-i\omega t}$ in the viscous fluid is expressed as follows:

$$\left(\nabla^2 + K^2\right)\vec{v} - \left(1 - \frac{K^2}{k^2}\right)\nabla\left(\nabla \cdot \vec{v}\right) = 0 \tag{7.1}$$

Here, $\vec{v}$ is the perturbation in the fluid velocity due to the acoustic field. K and k are the viscous-fluid propagation constants for shear and compressional modes:

$$K = \frac{\omega}{C_f} \qquad\qquad k = \frac{\omega}{c_f} \tag{7.2}$$

In the above expressions, C_f^2 and c_f^2 define the shear and compressional wave propagation constants, respectively:

$$C_f^2 = -i\omega\eta/\rho \qquad c_f^2 = \left(\frac{1}{\kappa} - 2i\omega\eta\right)\Big/\rho \tag{7.3}$$

Here, ρ, 1/κ, η are the density, compressibility, and the coefficient of viscosity of the fluid. Two scalar generating functions can be defined in terms of the two wave velocities, compressional and shear, as follows:

$$\vec{v}_c = \frac{-1}{k^2}\nabla\pi_c \qquad \vec{v}_s = \frac{1}{K}\nabla\times\nabla\times\vec{r}\pi_s \tag{7.4}$$

where the scalar generating functions can be shown to satisfy the scalar wave equation:

$$\left(\nabla^2 + k^2\right)\nabla\cdot\vec{v}_c = 0 \tag{7.5}$$

$$\nabla\cdot\vec{v}_c = \pi_c$$

$$\left(\nabla^2 + K^2\right)\pi_s = 0$$

By manipulating Equation 7.1, particular solutions for the compressional and shear waves in Equation 7.4 and expressions for the stress components, σ_{rr} and $\sigma_{r\theta}$, can be determined. The incident-plane compressional wave of unit amplitude may be expressed as follows:

$$\vec{v} = \hat{z}e^{ik_1 z} \tag{7.6}$$

where both the displacement and propagation of the incident wave occur in the z-direction. The incident wave is expanded in terms of spherical wave functions and expressed in terms of scalar

generating functions, permitted by the divergenceless nature of vectors $\vec{v}_c$ and $\vec{v}_s$. Continuity of three velocities as well as three stress components must be satisfied across the surface of the sphere to ensure that the two media remain in contact and equilibrium of an arbitrary volume which encloses portions of both media is maintained. In Equation 17 of Hinders' work, the scalar potential of the scattered compressional wave has amplitude (Δ_1/Δ_0), where the complicated solutions for Δ_1 and Δ_0 follow in Equation 20. (Equations 17 and 20 are presented in Appendix A.) This complex amplitude of the reflected wave is expressed in terms of Ricatti-Bessel, Ricatti-Hankel, and spherical Bessel functions of the first and second kinds. To test the coefficients of the scattered wave, it is demonstrated that in the limiting case of $\eta \rightarrow 0$, the solutions match those of the scattering of acoustic waves from nonviscous fluid sphere immersed in a nonviscous fluid medium (Anderson's formulation).

In order to generate frequency spectra for lipid emboli, the expressions (Δ_1/Δ_0) and (Δ_3/Δ_0) were implemented in MATLAB with the estimated input parameters presented in Table 7.1. (The MATLAB implementation of compressional and transverse scattering coefficients is presented as Programs 7.1 and 7.2 in Appendix B.)

Material	Dynamic Viscosity (Pa·s)	Compressibility (Pa^{-1})	Density (kg/m^3)	Acoustic Speed (m/s)
Blood	5×10^{-3}	4.55×10^{-10}	1060	1570
Lipid	0.799	6.2×10^{-10}	918	1455

Table 7.1 Estimated input parameters used to generate Figure 7.1 from Hinders's analysis [20].

The result was a frequency spectrum for 400-micron lipid emboli, shown in Figure 7.1. Unlike the corresponding curve from the non-viscous analysis, this spectrum has narrow resonance-like

structures. Figure 7.2 illustrates Anderson's reflectivity factor *R* from Equation 4.8 as a function of frequency in the range of 0 to 6MHz.

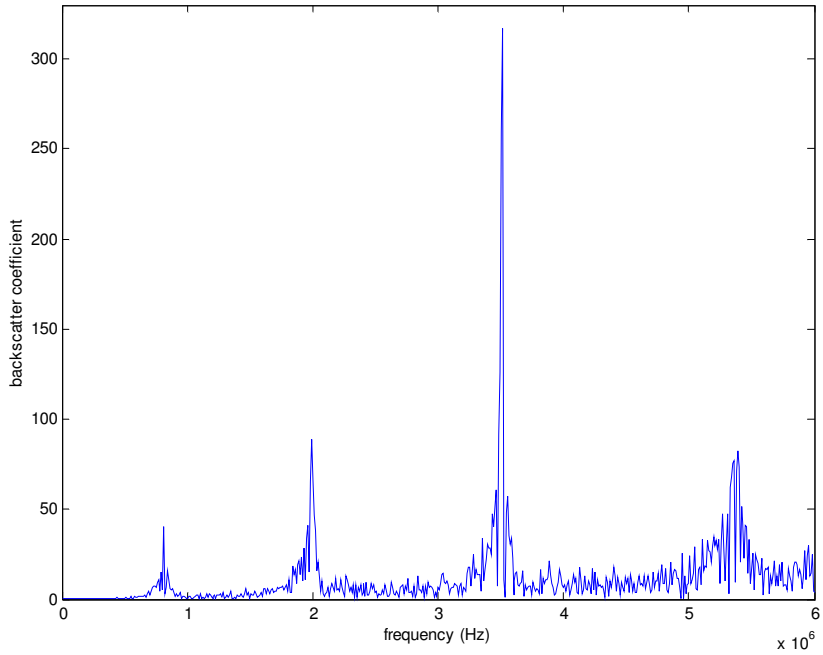

Figure 7.1 Scattered amplitude versus frequency for a 200-micron lipid embolus in blood using Hinders' viscous-fluid model [20].

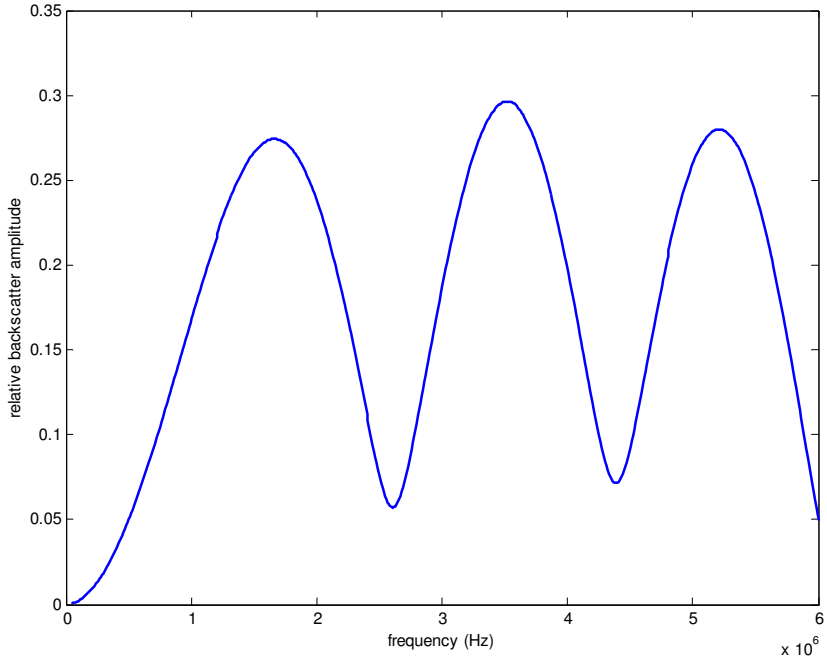

Figure 7.2 Scattering coefficients for a 200-micron lipid embolus in blood from Anderson's nonviscous-fluid model [11].

When Figures 7.1 and 7.2 are compared, there appear to be some similarities in the placement of peaks and resonances. Both graphs, for instance, have peaks at about 3.5MHz and just over 5MHz. The jaggedness of the curve generated using the viscous fluid model is likely the result of compounded numerical computation.

For the viscous fluid model to be applicable in a clinical setting, the viscosities of blood and lipid emboli must be precise. Viscosity values depend on temperature and vary widely according to different references, and when the dynamic viscosity input parameters are altered even slightly, the program output can change dramatically. When the viscosity coefficient of blood is increased by a thousandth, for example, the resonances shift and valid calculations cannot be completed for the entire frequency range. The scattering solutions for the viscous fluid model were implemented in MATLAB several different ways to test whether one implementation behaved in a more stable manner than another, but the same sensitivity was observed for each version. We conclude that this model is highly sensitive to the dynamic viscosity of the scatterer and surrounding fluid, and for further analysis, the viscosity values relevant to the particular clinical application need be specified.

Chapter 8: Acoustic Radiation Force Calculations

In a recent review article, Barak and Katz [2] cite several limitations and disadvantages of arterial filters in the prevention of microemboli in systemic circulation. First, the add-on to the circuit tubing increases resistance to blood flow, which has been demonstrated by a pressure drop through the filter. Following a short period of blood filtering, debris and fibrin within the blood flow saturate the filter, further increasing resistance. In severe cases, the used filter may completely block flow through the line, or chemicals within the filter may trigger a coagulation cascade and other biological reactions to foreign materials. In 2001 in Europe, fifty deaths of hemodialysis patients were linked to a solvent chemical that was used and not properly removed from the filters during the manufacturing process [2]. Pre- and post-monitoring the filter can assist clinicians in reducing some of the risks associated with filter saturation. However, it is useful to study additional microemboli management methods besides or in conjunction with the use of arterial filters. Recent development of optimal devices for microbubble elimination has focused on alternatives to mechanical obstructing filter designs. Schwarz *et al* [21] have demonstrated the possibility of using ultrasound to affect microbubbles in the bloodstream, while Schonburg *et al* have successfully evaluated the use of a dynamic bubble trap that directs and captures the bubbles at the center of the blood flow [22].

Currently we are using our scattering solutions as the basis for an exact analytical model to calculate the radiation force on emboli needed to optimize debubbling adjuncts to the EDAC device. The main principle for these debubbling adjuncts is to deliver an ultrasonic pulse to the microemboli in the blood flow, creating a unidirectional acoustic radiation force that pushes the microemboli out the blood flow so that the bubbles may be collected and thus prevented from entering the systemic circulation. We apply our scattering coefficients to two acoustic radiation force models to predict which frequencies would optimize the performance of these debubbling adjuncts.

In our first model, Lin and Raptis [23] study the scattering of a plane wave from an elastic, homogeneous, solid sphere immersed in an infinite, viscous, barotropic, compressible fluid. Similar to the Anderson and Hinders formulations, Lin and Raptis consider solutions to the boundary-value problem of acoustic-wave scattering in terms of spherical Bessel and Hankel functions with unknown coefficients for the refracted and scattered waves. The unknown coefficients are determined from boundary conditions at the interface of the sphere and fluid medium, with the coefficients of the scattered waves satisfying the radiation condition at infinity. Lin and Raptis calculate the pressure field at a large distance from the sphere:

$$p_s = \frac{P_0}{K_1 r}\left[\left(\frac{4\mu}{3}+k\right)K_1^2 - i\omega\rho_0\right]\times\sum_{m=0}^{\infty}(2m+1)A_m P_m(\cos\theta)e^{i(K_1 r-\pi/2)} \tag{8.1}$$

where P_0 is the pressure amplitude of the incident compressional wave traveling in the z-direction, K_1 is the compressional wave number in the viscous fluid, μ is the dynamic viscosity, k is the compressional wave number in the sphere, and A_m is the pressure amplitude of the scattered compressional wave. The angular distribution of normalized pressure amplitude for the scattered waves is expressed as follows:

$$\theta = \left[1+\left(\frac{4\nu}{3}+k_\nu\right)^2\frac{\omega^2}{c^4}\right]^{1/2}\times\left|\sum_{m=0}^{\infty}(2m+1)A_m P_m(\cos\theta)\right| \tag{8.2}$$

where θ is the azimuthal angle, ν is the kinematic viscosity, and k_ν is the ratio of bulk viscosity to the fluid density. By symmetry, the resultant force of acoustic radiation on the sphere's surface is in the z-direction and is given by

$$F = 2\pi a^2 \int_0^{\pi} \left(\sigma_{rr}\cos\theta - \sigma_{r\theta}\sin\theta\right)_{r=a} \sin\theta d\theta \tag{8.3}$$

where the shear-stress components σ_{rr} and $\sigma_{r\theta}$, identical to those in Hinders' formulation [20], are integrated over the fluid-sphere interface. The result can be expressed as follows:

$$F = 2\pi a^2 \omega\rho_0 P_0 \{6B_1 h_1(K_2 a) - 3[A_1 h_1(K_1 a) + j_1(K_1 a)]\} \tag{8.4}$$

where B_1 is the pressure amplitude of the scattered transverse wave and K_2 is the viscous wave number,

$$K_2 = (1+i)(\omega/2\nu)^{1/2}. \tag{8.5}$$

Note that only the $l = 1$ term remains in Equation 8.4. To obtain a dimensionless force function, the absolute value of this equation is divided by $\pi a^2 P_0$, so that we have the acoustic radiation force per unit area per unit pressure of the incident wave. This dimensionless force function was implemented in MATLAB for numerical computation (Program 8.1 in Appendix B).

For initial simplicity, the implemented force function was tested using the coefficients from Anderson's nonviscous fluid model. Specifically, the coefficients A_1 in Equation 8.4 were considered the $l = 1$ mode reflection coefficients for the case of scattering from a 200μm air embolus. Since the Anderson formulation accounts for nonviscous fluids that do not support transverse waves, the transverse scattering coefficient B_1 in Equation 8.4 was considered to approach zero. Figure 8.1 shows the dimensionless force function versus frequency for air in blood. Again, using the compressional scattering coefficients from the Anderson formulation, the dimensionless force function was plotted for a 200μm fat embolus in blood, shown in Figure 8.2.

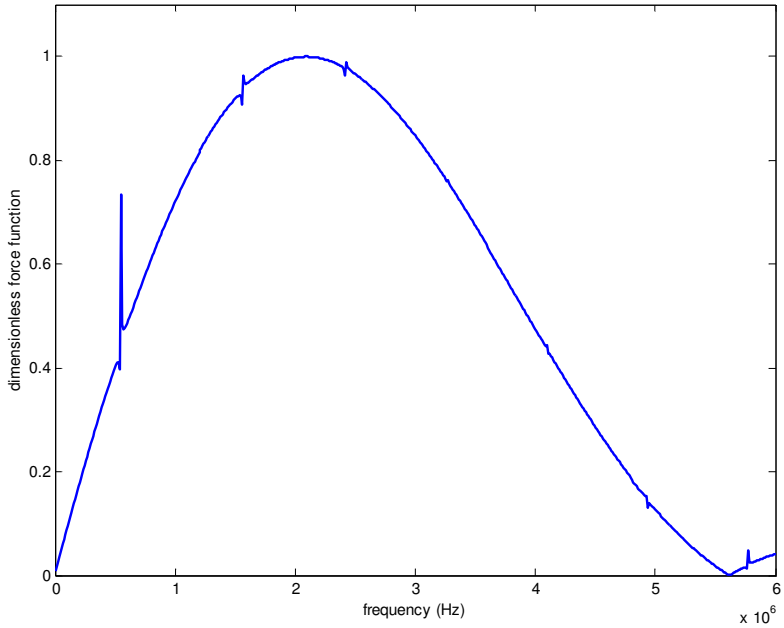

Figure 8.1 Dimensionless acoustic radiation force function for a 200-micron air embolus in blood, based on the analysis of Lin and Raptis [23].

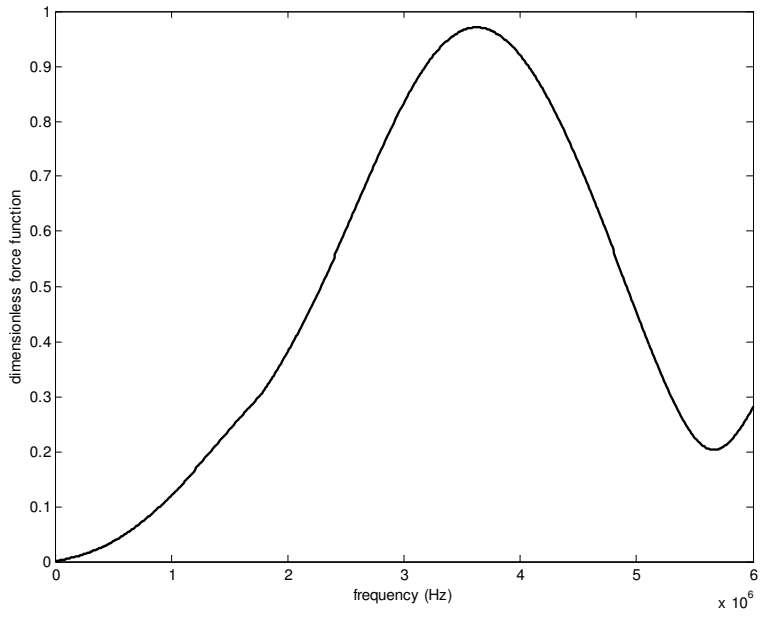

Figure 8.2 Dimensionless acoustic radiation force function for a 200-micron lipid embolus in blood, based on the analysis of Lin and Raptis [23].

In our second acoustic radiation force model, Hasegawa and Yosioka [24] calculate the force exerted by plane progressive waves on the surface of a solid, isotropic, elastic sphere immersed in a nonviscous fluid. The acoustic radiation force is expressed as follows:

$$\langle F \rangle = -\left\langle \iint_{S_0} \rho\left(q_n \vec{n} + q_t \vec{t}\right) q_n dS \right\rangle + \left\langle \iint_{S_o} \frac{1}{2} \rho q^2 \vec{n} dS \right\rangle - \left\langle \iint_{S_0} \frac{1}{2} \frac{\rho}{c^2} \phi^2 \vec{n} dS \right\rangle \qquad (8.6)$$

where S_0 is the boundary at its equilibrium position, $q = -\nabla\phi$ is the first-order particle velocity in the surrounding fluid, $\vec{n}$ and $\vec{t}$ are the outward normal and tangential unit vector components of dS, and < > is the notation representing a time average. Here, the radiation force is determined by integrating the time-averaged Brillouin radiation stress tensor over the scatterer's surface. For a spherical boundary of radius a and an axially symmetric acoustic field ($\theta = 0$), the radiation force is

$$< F > = < F_r > + < F_\theta > + < F_{r\theta} > + < F_t >, \qquad (8.7)$$

where

$$F_r = -\pi a^2 \rho \int_0^\pi \left(\frac{\partial \phi}{\partial r}\right)^2_{r=a} \sin\theta \cos\theta d\theta$$

$$F_\theta = \pi \rho \int_0^\pi \left(\frac{\partial \phi}{\partial \theta}\right)^2_{r=a} \sin\theta \cos\theta d\theta$$

$$F_{r\theta} = 2\pi a \rho \int_0^\pi \left(\frac{\partial \phi}{\partial r}\right)_{r=a} \left(\frac{\partial \phi}{\partial \theta}\right)_{r=a} \sin^2\theta d\theta$$

$$F_t = -\left(\frac{\pi a^2 \rho}{c^2}\right) \int_0^\pi \left(\frac{\partial \phi}{\partial r}\right)^2_{r=a} \sin^2\theta \cos\theta d\theta$$

and the velocity potential is of the form

$$\phi = \sum_{m=0}^{\infty} (2m+1)(-i)^m \left[U_m(kr) + iV_m(kr)\right] P_m(\cos\theta) e^{i\omega t}. \tag{8.8}$$

In these expressions, $U_m(kr)$ and $V_m(kr)$ are defined as follows:

$$U_m = j_m(kr)(1+\alpha_m) + \beta_m y_m(kr) \tag{8.9}$$

$$V_m = \beta_m j_m(kr) - \alpha_m y_m(kr)$$

where α_m and β_m are the real and imaginary components of the scattering coefficient of the scattered wave, respectively. After necessary manipulations, the four force components in Equation 8.7 can be written in terms of $U_m(kr)$, $V_m(kr)$, and their derivatives with respect to the acoustic radius kr. The mean energy density E in the incident field of unit amplitude is

$$E = \frac{1}{2}\rho k^2 \tag{8.10}$$

which we can use to define a dimensionless quantity Y_p, the radiation force per unit cross section and unit mean energy density:

$$Y_p = \frac{\langle F \rangle}{\pi a^2 E} \tag{8.11}$$

This term is referred to as the acoustic radiation force function. Writing Y_p in terms of Eqs. (8.7) – (8.10), the expansion for the acoustic radiation force function reduces to

$$Y_p = 4\sum_{m=0}^{\infty} (m+1)(\alpha_m + \alpha_{m+1} + 2\alpha_m\alpha_{m+1} + 2\beta_m\beta_{m+1}) \times \left[j_m(kr)y_m(kr) - j_{m+1}(kr)y_m(kr)\right]. \tag{8.12}$$

Using the following Wronskian for simplification,

$$(kr)^2\left[j_{m+1}(kr)y_m(kr)-j_m(kr)y_{m+1}(kr)\right]=1,$$

the acoustic radiation force function can be written as

$$Y_p=\frac{-4}{(kr)^2}\sum_{m=0}^{\infty}(m+1)(\alpha_m+\alpha_{m+1}+2\alpha_m\alpha_{m+1}+2\beta_m\beta_{m+1}). \qquad (8.13)$$

This force function was implemented in MATLAB for numerical computation (Program 8.2 in Appendix B), using Anderson's compressional scattering coefficients for air and fat emboli in blood. Hasegawa and Yosioka's acoustic radiation force function is plotted for air and fat in Figures 8.3 and 8.4, respectively.

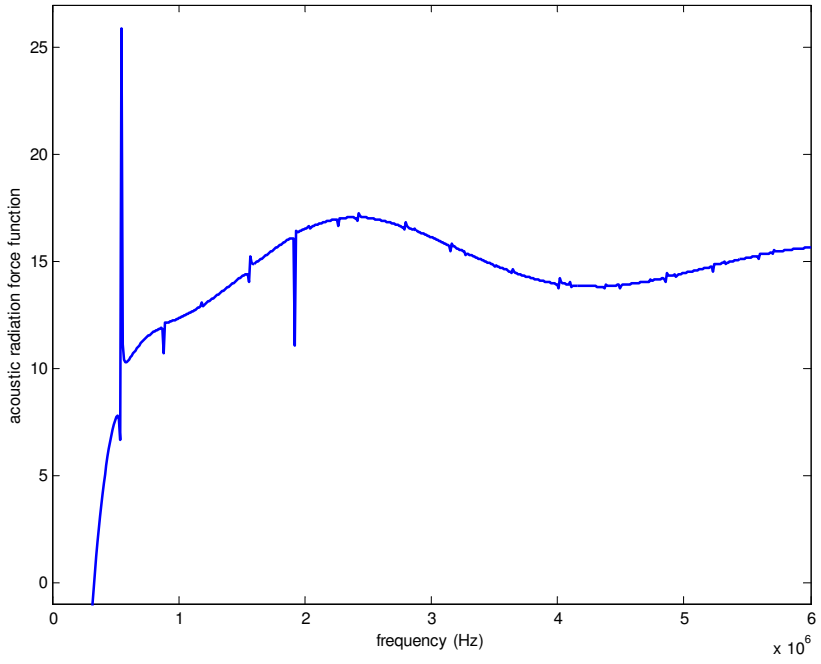

Figure 8.3 Dimensionless acoustic radiation force function for a 200-micron air embolus in blood, based on the analysis of Hasegawa and Yosioka [24].

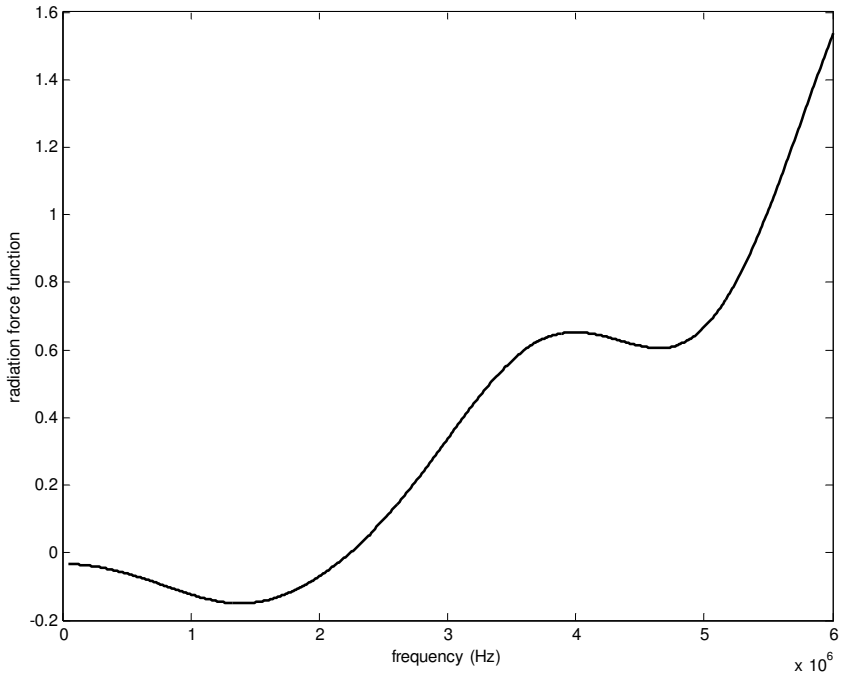

Figure 8.4 Dimensionless acoustic radiation force function for a 200-micron lipid embolus in blood, based on the analysis of Hasegawa and Yosioka [24].

For clarity in analyzing acoustic scattering and radiation force, Table 8.1 presented at the conclusion of the chapter provides a summary of scatterer and medium properties in each of the four models considered in this work. It should be noted that the numerical computations represented in Figures 8.1 to 8.4 are preliminary calculations, as they combine different aspects of these models that may or may not be most relevant to the emboli classification study. Since the dynamic viscosity values of fat and blood are not precisely specified, we begin by testing the acoustic radiation force functions with scattering coefficients from Anderson's nonviscous-fluid model. Since the characteristics of the Anderson model differ somewhat from those of the two radiation force models, we expect that these force functions will differ with scattering coefficients from other models.

The radiation force functions for a 200μm air bubble in blood according to the Lin and Raptis and the Hasegawa and Yosioka formulations are illustrated in Figures 8.1 and 8.3,

respectively. Although these curves differ in the range of 3.5-6MHz, there are several similarities in behavior below 3.5MHz. Both curves increase steadily from 0 to 2 MHz and feature a resonance structure at about 500 Hz. In addition, they both reach a maximum between 2-2.5 MHz. Figures 8.2 and 8.4 illustrate the radiation force functions for a 200μm fat embolus in blood according to the Lin and Raptis and the Hasegawa and Yosioka formulations, respectively. Like the corresponding graphs for air emboli, these lipid curves feature significantly different behavior in the range of about 4 – 6MHz. Both curves, however, increase to a local maximum just before 4MHz.

According to Figures 8.1 and 8.2 produced using Lin and Raptis' dimensionless force function, the radiation force function increases to a maximum within the range of 1 – 4MHz and then decreases in the range of 4 – 6MHz. For Hasegawa and Yosioka's acoustic radiation force function, the curve either continues oscillating or increases steadily beyond 5MHz. These variations in behavior for the two force functions are possibly due to the combination of nonviscous- and viscous-fluid models. Despite these differences, this preliminary analysis suggests that 2 – 2.5MHz and 3.5 – 4MHz may be optimal frequencies for generating maximum radiation force on air and fat emboli, respectively. Further studies and experimental data are needed to verify these findings.

Acoustic Scattering Models	**Anderson**	*Scatterer* Nonviscous fluid Compressible Modified to include attenuation Extended to account for scattering from a thin surrounding shell	*Medium* Nonviscous fluid Compressible Modified to include attenuation
	Hinders	*Scatterer* Viscous fluid or elastic solid	*Medium* Viscous fluid Compressible
Acoustic Radiation Force Models	**Lin and Raptis**	*Scatterer* Elastic solid	*Medium* Viscous fluid Compressible
	Hasegawa and Yosioka	*Scatterer* Elastic solid	*Medium* Nonviscous fluid Compressible

Table 8.1 Summary of the characteristics of each of the acoustic scattering and radiation force models utilized in this work.

Chapter 9: Discussion

Our work demonstrates that V.C. Anderson's steady-state analytical solutions for acoustic scattering from fluid spheres can be effectively applied to ultrasound scattering from emboli in the bloodstream. The formulation has been modified to account for attenuation in the fluid scatterer and surrounding medium, and the boundary conditions have been extended to characterize backscatter when a thin shell of material surrounds the spherical scatterer. We have demonstrated that our MATLAB implementation of this theoretical model is consistent with a two-dimension axisymmetric scattering simulation based on the cylindrical acoustical finite integration technique (CAFIT). In addition, this CAFIT simulation and analytical model have been used to validate the experimental observation that the pressure amplitude of a reflection from an air embolus in blood is linearly proportional to the scatterer's diameter. While the CAFIT simulations show that this assumption of a linear relationship between microemboli diameter and echo amplitude can produce sizing errors by as much as 20 percent, these sizing errors can be averaged out when performed over many counts. Additional variations due to an inhomogenous interrogating beam and other factors are also averaged by the EDAC's motion tracking algorithms that align and accumulate signals over 10 to 50 pulses, depending on the flow rate within the bypass circuit. While this method of sizing air emboli is optimal for the current EDAC system, the future possibility of a digitization rate higher than 48MHz would permit resolution of the resonance structures in the air emboli frequency spectra. Characterization of the resonance behavior would likely enable more accurate sizing of air emboli as well as identification of multi-layered emboli.

Currently we have not established a scheme for sizing lipid emboli, due to the relatively broad peaks in the frequency spectrum. Transducers with larger bandwidth are needed to link the size of lipid emboli to features in the frequency spectrum. Further studies of phase shift

could possibly reveal a means of sizing fat particles or distinguishing nongaseous emboli from air emboli.

As described in chapter 7, we have extended our scattering models to account for viscosity in the spherical scatterer and surrounding medium. The aim in using this model is to better characterize backscatter from emboli composed of lipids or soft solids. Since our implementation of the viscous-fluid model is quite sensitive to dynamic viscosity values, clinical specification of the relevant input parameters would provide for a more confident analysis. Similarly, a clinical description of the multi-layered emboli of interest would help guide our analysis of scattering from emboli with thin layers of surrounding material. Experimental data would additionally benefit this study. A current challenge in characterizing nongaseous emboli is deciding on the most appropriate model for this particular application. It is unclear, for instance, whether to use a viscous-fluid model or an elastic solid model for fatty material in the blood flow. The benefit of implementing a viscous-fluid model, however, is that it can be easily translated into a model for scattering from elastic solids. Future models may account for other factors such as thermal conduction or non-spherical embolic geometries.

To initiate a study of the optimal acoustic radiation force needed to remove emboli from the blood flow, we have implemented two radiation force models. The first model formulated by Lin and Raptis considers scattering from an elastic solid sphere immersed in a viscous fluid, in a manner similar to that of Anderson and Hinders. The radiation force, in this case, is determined by taking the time average of the integration of stress components over the scatterer's surface. The second model formulated by Hasegawa and Yosioka considers scattering from an elastic solid sphere immersed in nonviscous fluid. The scattering coefficients are found in a similar manner, and the radiation force function is determined by integrating the time-averaged Brillouin radiation stress tensor over the scatterer's surface. The preliminary graphs generating these two models suggest that 2 – 2.5MHz and 3.5 – 4MHz may be optimal frequencies for maximum

radiation force on air and fat emboli, respectively. Future experimental testing will direct our analysis and indicate the most appropriate models for emboli classification.

Acknowledgements

I would like to thank my research mentor, Professor Mark K. Hinders, for his constant guidance, support, and inspiration. I would like to extend gratitude to Dr. Ted E. Lynch for including me in the EDAC project at Luna Innovations, Inc. and for providing the experimental setup and analysis for this thesis. I would also like to thank Kevin E. Rudd for his guidance and the contribution of his CAFIT scattering simulations, and the National Science Foundation Research Experiences for Undergraduates program, for providing research funding during the summers of 2005 and 2006. Finally, I would like to express my gratitude to all the members of William and Mary's NDE lab for their support and for motivating me through their example.

References

[1] National Heart Lung and Blood Institute, Diseases and Conditions Index, http://www.nhlbi.nih.gov/health/dci/index.html (March 2007).

[2] M. Barak and Y. Katz, Chest 128, 2918-2932 (2005).

[3] T.S. Padayachee *et al,* Ann. Thorac. Surg. 45, 647-9 (1988).

[4] W. Pugsley *et al*, Stroke 25, 1393-9 (1994).

[5] M. Sellmen *et al*, Perfusion 5, 23-32 (1990).

[6] K.G. Shann *et al*, J. Thorac. Cardiovasc. Surg. 132(2), 283-290 (2006).

[7] B.D. Butler *et al*, Aviat. Space Environ. Med. 62(10), 997-1004 (1991).

[8] E.V. Van Zuilen *et al*, Stroke 27(10), 1840-3 (1996).

[9] T.S. Padayachee *et al,* Ann. Thorac. Surg. 44(3), 298-302 (1987).

[10] K. Tufan *et al*, Aviat. Space Environ. Med. 77(9), (2006).

[11] V.C. Anderson, J. Acoust. Soc. Am. 22, 426-431 (1950).

[12] R.A. Roy, R.E. Apfel, J. Acoust. Soc. Am. 87, 2332-2341 (1990).

[13] T.K. Stanton *et al*., J. Acoust. Soc. Am. 103, 225-235 (1998).

[14] R.K. Johnson, J. Acoust. Soc. Am. 61, 375-377 (1977).

[15] S.A. Goss, R.L. Johnston, and F. Dunn, J. Acoust. Soc. Am. 64, 423-430 (1973).

[16] S.A. Goss *et al*, J. Acoust. Soc. Am. 68, 93-99 (1980).

[17] P.N.T. Wells, Phys. Med. Biol. 22, 629-669 (1977).

[18] F. Schubert, B. Koehler, and A. Pieffer, J. Comp. Acoust. 9, 1127-1146 (2001).

[19] A. Peiffer *et al*, J. Acoust. Soc. Am. 102, 697-706 (1997).

[20] M.K. Hinders, Physical Review, 43A, #10, 5628-5637 (1991).

[21] K.Q. Schwarz *et al*, J. Thorac. Cardiovasc. Surg. 104, 1647-1653 (1992).

[22] M. Schonburg *et al*, Perfusion 16, 19-25 (2001).

[23] W.H. Lin and A.C. Raptis, J. Acoust. Soc. Am. 73(3), 736-748 (1983).

[24] T. Hasegawa and K. Yosioka, J. Acoust. Soc. Am. 46(5), 1139-1143.

Appendix A: Scattering Coefficients for the Viscous-Fluid Model

The following equations are taken directly from M.K. Hinders's *Extinction of sound by spherical scatterers in viscous fluid* [20]. Equation 17 contains expressions for the scalar potentials of incident, scattered, and transmitted waves. Equation 20 shows expressions for the scattering coefficients referred to in Equation 17. In these equations, $\psi_l(kr)$ and $\xi_l(kr)$ refer to the Ricatti-Bessel and Ricatti-Hankel functions, respectively. The scattering coefficients (Δ_1/Δ_0) and (Δ_3/Δ_0) were implemented in MATLAB, as shown in Appendix B, Programs 7.1 and 7.2.

$$r\pi_C^i = \sum_{l=0}^{\infty} i^{l+1}(2l+1)\psi_l(k_1 r)P_l(\cos\theta) ,$$

$$r\pi_C^s = \sum_{l=0}^{\infty} i^{l+1}(2l+1)\left[\frac{\Delta_1^f}{\Delta_0^f}\right]\zeta_l(k_1 r)P_l(\cos\theta) ,$$

$$r\pi_C^t = \sum_{l=0}^{\infty} i^{l+1}(2l+1)\left[\frac{\Delta_2^f}{\Delta_0^f}\right]\psi_l(k_2 r)P_l(\cos\theta) , \quad (17)$$

$$r\pi_S^s = \sum_{l=0}^{\infty} i^{l+1}(2l+1)\left[\frac{\Delta_3^f}{\Delta_0^f}\right]\zeta_l(K_1 r)P_l(\cos\theta) ,$$

$$r\pi_S^t = \sum_{l=0}^{\infty} i^{l+1}(2l+1)\left[\frac{\Delta_4^f}{\Delta_0^f}\right]\psi_l(K_2 r)P_l(\cos\theta) ,$$

$$\Delta_0^f = \left[\frac{\eta_2}{\eta_1}-1\right]^2 [l(l+1)-2]\left[\frac{k_2 a j_l'(k_2a)}{j_l(k_2a)}\frac{K_2 a\psi_l'(K_2a)}{\psi_l(K_2a)}-l(l+1)\right]\left[\frac{k_1 a h_l'(k_1a)}{h_l(k_1a)}\frac{K_1 a\xi_l'(K_1a)}{\xi_l(K_1a)}-l(l+1)\right]$$
$$+\tfrac{1}{2}(K_1a)^2\left[\frac{\eta_2}{\eta_1}-1\right]\left[\left[\frac{k_2 a j_l'(k_2a)}{j_l(k_2a)}\frac{K_2 a\psi_l'(K_2a)}{\psi_l(K_2a)}-l(l+1)\right]\left[\frac{K_1 a\xi_l'(K_1a)}{\xi_l(K_1a)}+2\frac{k_1 a h_l'(k_1a)}{h_l(k_1a)}-2l(l+1)\right]\right.$$
$$\left.-\frac{\rho_2}{\rho_1}\left[\frac{k_1 a h_l'(k_1a)}{h_l(k_1a)}\frac{K_1 a\xi_l'(K_1a)}{\xi_l(K_1a)}-l(l+1)\right]\left[\frac{K_2 a\psi_l'(K_2a)}{\psi_l(K_2a)}+2\frac{k_2 a j_l'(k_2a)}{j_l(k_2a)}-2l(l+1)\right]\right]$$
$$+\tfrac{1}{4}(K_1a)^4\left[l(l+1)\left[1-\frac{\rho_2}{\rho_1}\right]^2-\left[\frac{k_2 a j_l'(k_2a)}{j_l(k_2a)}-\frac{\rho_2}{\rho_l}\frac{k_1 a h_l'(k_1a)}{h_l(k_1a)}\right]\left[\frac{K_2 a\psi_l'(K_2a)}{\psi_l(K_2a)}-\frac{\rho_2}{\rho_1}\frac{K_1 a\xi_l'(K_1a)}{\xi_l(K_1a)}\right]\right], \tag{20a}$$

$$\Delta_l^f = \frac{j_l(k_1a)}{h_l(k_1a)}\left\{\left[\frac{\eta_2}{\eta_1}-1\right]^2[l(l+1)-2]\left[\frac{k_2 a j_l'(k_2a)}{j_l(k_2a)}\frac{K_2 a\psi_l'(K_2a)}{\psi_l(K_2a)}-l(l+1)\right]\left[\frac{k_1 a j_l'(k_1a)}{j_l(k_1a)}\frac{K_1 a\xi_l'(K_1a)}{\xi_l(K_1a)}-l(l+1)\right]\right.$$
$$+\tfrac{1}{2}(K_1a)^2\left[\frac{\eta_2}{\eta_1}-1\right]\left[\left[\frac{k_2 a j_l'(k_2a)}{j_l(k_2a)}\frac{K_2 a\psi_l'(K_2a)}{\psi_l(K_2a)}-l(l+1)\right]\left[\frac{K_1 a\xi_l'(K_1a)}{\xi_l(K_1a)}+2\frac{k_1 a j_l'(k_1a)}{j_l(k_1a)}-2l(l+1)\right]\right.$$
$$-\frac{\rho_2}{\rho_1}\left[\frac{k_1 a j_l'(k_1a)}{j_l(k_1a)}\frac{K_1 a\xi_l'(K_1a)}{\xi_l(K_1a)}-l(l+1)\right]\left[\frac{K_2 a\psi_l'(K_2a)}{\psi_l(K_2a)}+2\frac{k_2 a j_l'(k_2a)}{j_l(k_2a)}\right.$$
$$\left.\left.\left.-2l(l+1)\right]\right]$$
$$+\tfrac{1}{4}(K_1a)^4\left[l(l+1)\left[1-\frac{\rho_2}{\rho_1}\right]^2\right.$$
$$\left.\left.-\left[\frac{k_2 a j_l'(k_2a)}{j_l(k_2a)}-\frac{\rho_2}{\rho_1}\frac{k_1 a j_l'(k_1a)}{j_l(k_1a)}\right]\left[\frac{K_2 a\psi_l'(K_2a)}{\psi_l(K_2a)}-\frac{\rho_2}{\rho_1}\frac{K_1 a\xi_l'(K_1a)}{\xi_l(K_1a)}\right]\right]\right\}, \tag{20b}$$

$$\Delta_2^f = \frac{j_l(k_1a)}{j_l(k_2a)}\left[\frac{k_1 a h_l'(k_1a)}{h_l(k_1a)}-\frac{k_1 a j_l'(k_1a)}{j_l(k_1a)}\right]$$
$$\times\left\{\frac{1}{4}(K_1a)^4\left[\frac{k_2 a\psi_l'(K_2a)}{\psi_l(K_2a)}-\frac{\rho_2}{\rho_1}\frac{K_1 a\xi_l'(K_1a)}{\xi_l(K_1a)}\right]\right.$$
$$\left.+\tfrac{1}{2}(K_1a)^2\left[\frac{\eta_2}{\eta_1}-1\right]\left[\frac{K_1 a\xi_l'(K_1a)}{\xi_l(K_1a)}\frac{K_2 a\psi_l'(K_2a)}{\psi_l(K_2a)}-l(l+1)\left[\frac{K_1 a\xi_l'(K_1a)}{\xi_l(K_1a)}+\frac{K_2 a\psi_l'(K_2a)}{\psi_l(K_2a)}-2\right]\right]\right\}, \tag{20c}$$

$$\Delta_3^f = \frac{K_1}{k_1}\frac{j_l(k_1a)}{h_l(K_1a)}\left[\frac{k_1 a j_l'(k_1a)}{j_l(k_1a)}-\frac{k_1 a h_l'(k_1a)}{h_l(k_1a)}\right]$$
$$\times\left\{\frac{1}{4}(K_1a)^4\left[\frac{\eta_2}{\eta_1}-1\right]\frac{\rho_2}{\rho_1}\left[1-\frac{\rho_2}{\rho_2}\right]\right.$$
$$+\tfrac{1}{2}(K_1a)^2\left[\frac{\eta_2}{\eta_1}-1\right]\left[\left[\frac{k_2 a j_l'(k_2a)}{j_l(k_2a)}\frac{K_2 a\psi_l'(K_2a)}{\psi_l(K_2a)}-l(l+1)\right]\right.$$
$$\left.\left.-\frac{\rho_2}{\rho_1}\left[\frac{K_2 a\psi_l'(K_2a)}{\psi_l(K_2a)}+2\frac{k_2 a j_l'(k_2a)}{j_l(k_2a)}-2l(l+1)\right]\right]$$
$$\left.+\left[\frac{\eta_2}{\eta_1}-1\right]^2[l(l+1)-2]\left[\frac{k_2 a j_l'(k_2a)}{j_l(k_2a)}\frac{K_2 a\psi_l'(K_2a)}{\psi_l(k_2a)}-l(l+1)\right]\right\}, \tag{20d}$$

Appendix B: Code for Functions Implemented in MATLAB

Program 4.1: V.C. Anderson's reflectivity factor

```
function [ R ] = reflect2f(r,alphm,alphe,cmed,cemb,g);
% V.C. Anderson's Reflectivity Factor Plotted as a Function of Frequency
% Alison Pouch  - The College of William and Mary

% Input Parameters
%--------------------------------------------------------------------------

% r = scatterer radius in meters
% alphm = attenuation coefficient of medium in Np/m
% alphe = attenuation coefficient of scatterer in Np/m
% cmed = acoustic speed of medium in m/s
% cemb = acoustic speed of scatterer in m/s
% g = relative density = density of scatterer / density of medium

% Other Parameters
%--------------------------------------------------------------------------

f = (2:0.01:6)*1E6;  %transducer frequency in Hz

kr(1,1:length(f))=r*[(2*pi*f./cmed)+f.*alphm*i*1e-6];   %acoustic radius of medium
kre(1,1:length(f))=r*[(2*pi*f./cemb)+f.*alphe*i*1e-6];  %acoustic radius of embolus
h(1,1:length(f))=kr./kre;                               %relative acoustic speed

% Reflectivity Factor and Frequency Spectrum Plot
%--------------------------------------------------------------------------

for m=0:50
    C(1,1:length(f))=[[alpha(m,kre)./alpha(m,kr)].*[besselsphy(m,kr)./besselsphj(m,kre)]-...
                      [beta(m,kr)./alpha(m,kr)].*g.*h]./[[alpha(m,kre)./alpha(m,kr)]
                       .*[besselsphj(m,kr)./besselsphj(m,kre)]-g.*h];
    U(m+1,1:length(f))=(2./kr).*([((-1)^m)*(2*m+1)]./[1+i*C]);
end

R = sum(U);
plot(f,abs(R));

%--------------------------------------------------------------------------
%--------------------------------------------------------------------------



%--------------------------------------------------------------------------
                      REQUIRED FUNCTIONS

%--------------------------------------------------------------------------
function [ J ] = besselsphj(m,kr)
% Spherical Bessel Function of the First Kind

% Input Parameters
%--------------------------------------------------------------------------
% m = order of spherical Bessel function
% kr = acoustic radius (dimensionless)

%--------------------------------------------------------------------------

J = [sqrt(pi./(2*kr))].*[besselj(m+.5,kr)];

%--------------------------------------------------------------------------
%--------------------------------------------------------------------------



function [ Y ] = besselsphy(m,kr)
% Spherical Bessel Function of the Second Kind

% Input Parameters
%--------------------------------------------------------------------------
```

```
% m = order of spherical Bessel function
% kr = acoustic radius (dimensionless)

%-------------------------------------------------------------------------

Y = [sqrt(pi./(2*kr))].*[bessely(m+.5,kr)];

%-------------------------------------------------------------------------
%-------------------------------------------------------------------------



function [ S ] = alpha(m,kr)
% Recursively-Defined Derivative of the Spherical Bessel Function of
% the the First Kind with respect to the argument kr

% Input Parameters
%-------------------------------------------------------------------------
% m = order of spherical Bessel function
% kr = acoustic radius (dimensionless)

%-------------------------------------------------------------------------

S(1,1:length(kr)) = m*besselsphj(m-1,kr)-(m+1)*besselsphj(m+1,kr);

%-------------------------------------------------------------------------
%-------------------------------------------------------------------------


function [ T ] = beta(m,kr)
% Recursively-Defined Derivative of the Spherical Bessel Function of
% the the Second Kind with respect to the argument kr

% Input Parameters
%-------------------------------------------------------------------------
% m = order of spherical Bessel function
% kr = acoustic radius (dimensionless)

%-------------------------------------------------------------------------

T(1,1:length(kr)) = m*besselsphy(m-1,kr)-(m+1)*besselsphy(m+1,kr);

%-------------------------------------------------------------------------
%-------------------------------------------------------------------------
```

Program 4.2: Scattering coefficients for a spherical scatterer with thin surrounding shell

```
function [ A ] = am(a,b,c1,d1,a1,c2,d2,a2,c3,d3,a3);
% Compressional Scattering Coefficients of a Reflection from a Spherical Scatterer
% Surrounded by a Thin Shell (An Extension of V.C. Anderson's Scattering Model)
% Alison Pouch  - The College of William and Mary

% Input Parameters
%-------------------------------------------------------------------------

% Subcripts:   1 --> medium    2 --> surrounding shell    3 --> spherical scatterer

% a = radius of spherical shell without shell in meters
% b = radius of spherical shell with shell in meters
% a1, a2, a3 = attenuation coefficient in Np/m
% c1, c2, c3 = acoustic speed in m/s
% d1, d2, d3 = density in kg/m^3

% Other Parameters
%-------------------------------------------------------------------------
f=2:1e-3:8;     % transducer frequency in MHz

% Acoustic Radii
x1(1,1:length(f))=a*[(2*pi*f./c1)+f.*a1*i*1e-6];
x2(1,1:length(f))=a*[(2*pi*f./c2)+f.*a2*i*1e-6];
x3(1,1:length(f))=a*[(2*pi*f./c3)+f.*a3*i*1e-6];
```

```
y1(1,1:length(f))=b*[(2*pi*f./c1)+f.*a1*i*1e-6];
y2(1,1:length(f))=b*[(2*pi*f./c2)+f.*a2*i*1e-6];

% Relative Impedances
z21=(d2*c2)/(d1*c1);
z23=(d2*c2)/(d3*c3);

% Scattering Coefficients
%--------------------------------------------------------------------------

for m = 0:50

    % Denominator of scattering coefficient
    delta0 = hankel1(m,y1).*((hankel2(m,x2)./hankel1(m,x2)).*(bigh1(m,y2)-
             z21*bigh1(m,y1)).*(bigh2(m,x2)-z23*bigj(m,x3))...
               -(hankel2(m,y2)./hankel1(m,y2)).*(bigh2(m,y2)
               -z21*bigh1(m,y1)).*(bigh1(m,x2)-z23*bigj(m,x3)));

    % Numerator of scattering coefficient
    delta1 = ((-1)^m)*(2*m+1)*(2./(y1)).*besselsphj(m,y1).*((hankel2(m,x2)./hankel1(m,x2))
              .*(bigh1(m,y2)-z21*bigj(m,y1)).*(bigh2(m,x2)-z23*bigj(m,x3))-
              (hankel2(m,y2)./hankel1(m,y2)).*(bigh2(m,y2)-z21*bigj(m,y1)).*(bigh1(m,x2)-
              z23*bigj(m,x3)));

    % Scattering coefficients
    d10(m+1,1:length(f)) = delta1./delta0;

end

A = sum(d10);
plot(f,abs(A));

%--------------------------------------------------------------------------
%--------------------------------------------------------------------------



%--------------------------------------------------------------------------
                      REQUIRED FUNCTIONS

%--------------------------------------------------------------------------

function [ j ] = bigj(m,kr);
% Function of Spherical Bessel Functions of the First Kind and their Derivatives

% Input Parameters
%--------------------------------------------------------------------------
% m = order of spherical Bessel function
% kr = acoustic radius (dimensionless)

%--------------------------------------------------------------------------

j = alpha(m,kr)./besselsphj(m,kr);

%--------------------------------------------------------------------------
%--------------------------------------------------------------------------



function [ y ] = bigy(m,kr);
% Function of Spherical Bessel Functions of the First Kind and their Derivatives

% Input Parameters
%--------------------------------------------------------------------------
% m = order of spherical Bessel function
% kr = acoustic radius (dimensionless)

%--------------------------------------------------------------------------

y = beta(m,kr)./besselsphy(m,kr);

%--------------------------------------------------------------------------
%--------------------------------------------------------------------------
```

```
function [ H ] = hankel1(m,kr)
% Spherical Hankel Function of the First Kind

% Input Parameters
%--------------------------------------------------------------------------
% m = order of Hankel function
% kr = acoustic radius (dimensionless)

%--------------------------------------------------------------------------

H = besselsphj(m,kr)+i*besselsphy(m,kr);

%--------------------------------------------------------------------------
%--------------------------------------------------------------------------


function [ h ] = hankel2(m,kr)
% Spherical Hankel Function of the Second Kind

% Input Parameters
%--------------------------------------------------------------------------
% m = order of Hankel function
% kr = acoustic radius (dimensionless)

%--------------------------------------------------------------------------

h = besselsphj(m,kr)-i*besselsphy(m,kr);

%--------------------------------------------------------------------------
%--------------------------------------------------------------------------



function [ h ] = bigh1(m,kr)
% Function of Spherical Hankel Functions of the First Kind and their Derivatives

% Input Parameters
%--------------------------------------------------------------------------
% m = order of spherical Bessel function
% kr = acoustic radius (dimensionless)

%--------------------------------------------------------------------------

h = (alpha(m,kr)+i*beta(m,kr))./(besselsphj(m,kr)+i*besselsphy(m,kr));

%--------------------------------------------------------------------------
%--------------------------------------------------------------------------


function [ h ] = bigh2(m,kr)
% Function of Spherical Hankel Functions of the Second Kind and their Derivatives

% Input Parameters
%--------------------------------------------------------------------------
% m = order of spherical Bessel function
% kr = acoustic radius (dimensionless)

%--------------------------------------------------------------------------

h = (alpha(m,kr)-i*beta(m,kr))./(besselsphj(m,kr)-i*besselsphy(m,kr));

%--------------------------------------------------------------------------
%--------------------------------------------------------------------------
```

Program 4.3: CAFIT simulations

```
function [ Aline ] = cafit_anyw( waveform, insr, scat_rad )
% Sample Cylindrical Acoustical Finite Integration Technique
% Kevin Rudd  - The College of William and Mary - 6/14/06
```

```
% Transducer Parameters
%-------------------------------------------------------------------------
%tfreq  = 3.9E6;%6E6    % transducer frequency in Hz (<= fmax)
trad   = 0.005;         % transducer radius in meters
%pulsecycles = 15;      % number of cycles in the initial tone burst

% Rigid Sphere Scatterer Parameters
%-------------------------------------------------------------------------
scat_zpos = 0.01;         % z position of rigid spere scatter in meters (<= zsize)
%scat_rad  = 0.000110;    % radius of rigid sphere scatterer            (<= rsize)
scat_c    = 331;          % sound of speed in scatterer
scat_d    = 1.29;         % density of scatterer
% Simulation Space Parameters
%-------------------------------------------------------------------------
zsize = 0.02;%0.015        % z-spatial size in meters
rsize = 0.008;%0.005       % r-spatial size in meters
tsize = 0.000016;          % time length of simulation in seconds

c    = 1570;           % speed of sound in medium
den  = 1060;           % density
fmax = 6E6; %3.5E6     % maximum frequency in simulation

% Other Parameters
%-------------------------------------------------------------------------
plotevery = 10;     % plots the pressure field every <plotevery> timesteps
abc       = 50;     % absorbing boundary width


%=========================================================================

cmax = max([c,scat_c]);      % max wavespeed in simulation
dz = (1/10)*(cmax/fmax);     % spatial step size: 10 grid points per wavelength
dt = (1/2)*dz/(cmax*sqrt(2)) % temporal step size

numr = round(rsize/dz)     % number of steps in the r-direction
numz = round(zsize/dz)     % number of steps in the z-direction
numt = round(tsize/dt)     % number of time steps

vr(1:numr,1:numz) = 0;     % r-velocity values
vz(1:numr,1:numz) = 0;     % z-velocity values
p(1:numr,1:numz)  = 0;     % pressure values

cc(1:numr,1:numz) = c;     % speed of sound matrix
dd(1:numr,1:numz) = den;   % density matrix

rs = [2:numr-1];
zs = [2:numz-1];
diagr = diag(1./(2.*rs));

% Sphere Scatter
for z = [round((scat_zpos-scat_rad)/dz):1:round((scat_zpos+scat_rad)/dz)]
    rrun = round( sqrt((scat_rad/dz)^2 - (scat_zpos/dz-z)^2) );
      if rrun >=1
        cc(1:rrun,z)=scat_c;
        dd(1:rrun,z)=scat_d;
      end
end

c2ddtodz = cc.*cc.*dd.*(dt/dz);
dtodz    = (dt/dz);

sampsin = [1:length(waveform)]*1/insr;
sampout = [0:dt:sampsin(end)];
ToneBurst = interp1(sampsin,waveform,sampout);
ToneBurst = ToneBurst./max(ToneBurst);
ToneBurst(isnan(ToneBurst)) = 0;

plot(ToneBurst);

numrtrans = round(trad/dz);
% Run the simulation
for t = 1:numt
    t=t
    % Drive Function
```

```
    if t<length(ToneBurst)
        vz(1:numrtrans,1) = ToneBurst(t);
        %ToneBurst(t)
    end

    % Update the Pressure Values
    p(rs,zs) = p(rs,zs) - c2ddtodz(rs,zs).*( (vr(rs,zs)-vr(rs-1,zs)) + (vz(rs,zs)-vz(rs,zs-1)) +
               diagr*(vr(rs,zs)+vr(rs-1,zs)) );
    p(1, zs) = p(1, zs) - c2ddtodz(1, zs).*( 2*vr(1,zs) + (vz(1,zs)-vz(1,zs-1) ) );

    % Update the Velocity Values
    vr([1, rs],zs)= vr([1, rs],zs) - 2*dtodz./(dd([1, rs],zs)+dd([1, rs]+1,zs)).*( (p([1,
                    rs]+1,zs)-p([1, rs],zs)) );
    vz([1, rs],zs)= vz([1, rs],zs) - 2*dtodz./(dd([1, rs],zs)+dd([1, rs],zs+1)).*( (p([1,
                    rs],zs+1)-p([1, rs],zs)) );

    % Absorbing Boundary Conditions
    vr([numr-abc:numr],zs)=diag(1-[0:abc]*.007)*vr([numr-abc:numr],zs);
    vz([numr-abc:numr],zs)=diag(1-[0:abc]*.007)*vz([numr-abc:numr],zs);
    vr([1:numr-abc],[numz-abc:numz]) = vr([1:numr-abc],[numz-abc:numz])*diag(1-[0:abc]*.007);
    vz([1:numr-abc],[numz-abc:numz]) = vz([1:numr-abc],[numz-abc:numz])*diag(1-[0:abc]*.007);

    % Collect Aline
    %Aline(t) = mean(vz(1:numrtrans,2));
    Aline(t) = mean(vz(1,2));

    % Plot the pressure values
    if rem(t,plotevery)==0
       h = pcolor([1:numz]*dz,[-numr:-1, 1:numr]*dz, [flipud(p); p]);
       set(h,'linestyle','none','FaceColor','interp'); axis equal; caxis([-1500000 1500000]);
       xlabel('z-distance (meters)'); ylabel('r-distance (meters)');
       [XX,YY] = pol2cart([0:pi/50:2*pi],scat_rad); line(XX+scat_zpos,YY);
       pause(.01);
    end
end

%sampsin = [1:length(Aline)]*dt;
%sampout = [0:1/(insr):sampsin(end)];
%Aline = interp1(sampsin,Aline,sampout);
%Aline(isnan(Aline)) = 0;
%Aline=Aline-mean(Aline);

%=========================================================================
```

Program 7.1: M.K. Hinders's [20] viscous-fluid compressional scattering coefficients

```
function [ S ] = scat3(r,a,d1,d2,kapinv1,kapinv2,n1,n2,c1,c2)
% M.K. Hinders's Scattering Coefficients for Compressional Waves
% Alison Pouch  - The College of William and Mary

% Input Parameters
%-------------------------------------------------------------------------

% Subcripts:   1 --> medium    2 --> scatterer

% a = scatterer radius in meters
% d = density  in kg/m^3
% kapinv = compressibility in 1/Pa
% n = coefficient viscosity in Pa*sec
% c = acoustic speed in m/s

% Other Parameters
%-------------------------------------------------------------------------

f = (0.01:0.01:6)*1E6;  % transducer frequency in Hz
omega = 2*pi*f;         % angular frequency in rad/sec

% Viscous-fluid propagation constants
Cfsq1 = -i*omega*n1/d1;
Cfsq2 = -i*omega*n2/d2;

cfsq1 = (kapinv1-2*i*omega*n1)/d1;
cfsq2 = (kapinv2-2*i*omega*n2)/d2;
```

```
K1 = omega./[(Cfsq1).^(1/2)];
K1a = K1*a;
K2 = omega./[(Cfsq2).^(1/2)];
K2a = K2*a;
k1 = omega./[(cfsq1).^(1/2)];
k1a = k1*a;
k2 = omega./[(cfsq2).^(1/2)];
k2a = k2*a;

nr = n2/n1;    % relative viscosity
dr = d2/d1;    % relative density

% Products of acoustic radii
Kk1 = k1a.*K1a;
Kk2 = k2a.*K2a;

% Scattering Coefficients
%--------------------------------------------------------------------------

for l = 0:50
    g2 = l*(l+1);
    X = g2*((1-dr)^2);
    M = [(n2-n1)^2]*[g2-2];
    N(1,1:length(f)) = (1/2)*(n2*n1-n1^2)*((K1a).^2);
    W(1,1:length(f)) = (1/4)*((K1a).^4);
    C(l+1,1:length(f)) = Kk2.*alpha(l,k2a).*dpsil(l,K2a)/(2*l+1)-
                         g2*besselsphj(l,k2a).*psil(l,K2a);
    D(l+1,1:length(f)) = K2a.*dpsil(l,K2a).*xi(l,K1a)-dr*K1a.*dxi(l,K1a).*psil(l,K2a);
    E(l+1,1:length(f)) = Kk1.*(alpha(l,k1a)+i*beta(l,k1a)).*dxi(l,K1a)/(2*l+1)-
                         g2*hankel1(l,k1a).*xi(l,K1a);
    F(l+1,1:length(f)) = K2a.*dpsil(l,K2a).*besselsphj(l,k2a)+2*k2a.*alpha(l,k2a)
                         .*psil(l,K2a)/(2*l+1)-2*g2*besselsphj(l,k2a).*psil(l,K2a);
    H(l+1,1:length(f)) = Kk1.*alpha(l,k1a).*dxi(l,K1a)/(2*l+1)-g2*besselsphj(l,k1a).*xi(l,K1a);

    % Numerator of the compressional scattering coefficient
    del1(l+1,1:length(f)) = [M.*C(l+1,1:length(f)).*H(l+1,1:length(f))+...
                             N.*[C(l+1,1:length(f)).*(K1a.*dxi(l,K1a).*besselsphj(l,k1a)
                             +2*k1a.*alpha(l,k1a).*xi(l,K1a)/(2*l+1)
                               -2*g2*besselsphj(l,k1a).*xi(l,K1a))-
                             dr*H(l+1,1:length(f)).*F(l+1,1:length(f))]+...
                               W*n1^2.*[X*besselsphj(l,k1a).*besselsphj(l,k2a).*psil(l,K2a)
                               .*xi(l,K1a)
            -D(l+1,1:length(f)).*(k2a.*alpha(l,k2a).*besselsphj(l,k1a)/(2*l+1)...
            -dr*k1a.*alpha(l,k1a).*besselsphj(l,k2a)/(2*l+1))]];

    % Denominator of the compressional scattering coefficient
    % The trivial quantity 1E-30(1+i) is added to avoid a divide-by-zero error
    del0(l+1,1:length(f)) = 1E-30*(1+i) + [M.*C(l+1,1:length(f)).*E(l+1,1:length(f))+...
        N.*[C(l+1,1:length(f)).*(K1a.*dxi(l,K1a).*hankel1(l,k1a)...
            +2*k1a.*(alpha(l,k1a)+i*beta(l,k1a)).*xi(l,K1a)/(2*l+1)...
            -2*g2*hankel1(l,k1a).*xi(l,K1a))-dr*E(l+1,1:length(f)).*F(l+1,1:length(f))]+...
        W*n1^2.*[X*hankel1(l,k1a).*besselsphj(l,k2a).*psil(l,K2a).*xi(l,K1a)...
            -D(l+1,1:length(f)).*(k2a.*alpha(l,k2a).*hankel1(l,k1a)/(2*l+1)...
            -dr*k1a.*(alpha(l,k1a)+i*beta(1,k1a).*besselsphj(l,k2a)/(2*l+1)))]];

end

Sl = del1./del0;
S = sum(Sl);

%--------------------------------------------------------------------------
%--------------------------------------------------------------------------
```

```
%-------------------------------------------------------------------------
                      REQUIRED FUNCTIONS
%-------------------------------------------------------------------------

function [ P ] = psil(l,kr)
% Ricatti-Bessel Function

% Input Parameters
%-------------------------------------------------------------------------
% l = order of spherical Bessel function
% kr = acoustic radius (dimensionless)

%-------------------------------------------------------------------------

P(1,1:length(kr)) = kr.*besselsphj(l,kr);

%-------------------------------------------------------------------------
%-------------------------------------------------------------------------


function [ d ] = dpsil(l,kr)
% Derivative of the Ricatti-Bessel Function

% Input Parameters
%-------------------------------------------------------------------------
% l = order of spherical Bessel function
% kr = acoustic radius (dimensionless)

%-------------------------------------------------------------------------

d(1,1:length(kr)) = (kr).*alpha(l,kr)/(2*l+1)+besselsphj(l,kr);

%-------------------------------------------------------------------------
%-------------------------------------------------------------------------


function [ x ] = xi(l,kr);
% Ricatti-Hankel Function

% Input Parameters
%-------------------------------------------------------------------------
% l = order of spherical Bessel function
% kr = acoustic radius (dimensionless)

%-------------------------------------------------------------------------

x(1,1:length(kr)) = kr.*[besselsphj(l,kr)+i*besselsphy(l,kr)];

%-------------------------------------------------------------------------
%-------------------------------------------------------------------------
function [ d ] = dxi(l,kr);
% Derivative of Ricatti-Hankel Function

% Input Parameters
%-------------------------------------------------------------------------
% l = order of spherical Bessel function
% kr = acoustic radius (dimensionless)

%-------------------------------------------------------------------------

d(1,1:length(kr)) =
[(kr)/(2*l+1)].*(alpha(l,kr)+i*beta(l,kr))+besselsphj(l,kr)+i*besselsphy(l,kr);

%-------------------------------------------------------------------------
%-------------------------------------------------------------------------
```

Program 7.2: M.K. Hinders's [20] viscous-fluid transverse scattering coefficients

```
function [ S ] = scatshear(r,a,d1,d2,kapinv1,kapinv2,n1,n2,c1,c2)
% M.K. Hinders's Scattering Coefficients for Transverse Waves
```

```
% Alison Pouch  - The College of William and Mary

% Input Parameters
%--------------------------------------------------------------------------

% Subcripts:   1 --> medium    2 --> scatterer

% a = scatterer radius in meters
% d = density  in kg/m^3
% kapinv = compressibility in 1/Pa
% n = coefficient viscosity in Pa*sec
% c = acoustic speed in m/s

% Other Parameters
%--------------------------------------------------------------------------

f = (0.01:0.01:6)*1E6;  % transducer frequency in Hz
omega = 2*pi*f;         % angular frequency in rad/sec

% Viscous-fluid propagation constants
Cfsq1 = -i*omega1*n1/d1;
Cfsq2 = -i*omega2*n2/d2;

cfsq1 = (kapinv1-2*i*omega1*n1)/d1;
cfsq2 = (kapinv2-2*i*omega2*n2)/d2;

K1 = omega./[(Cfsq1).^(1/2)];
K1a = K1*a;
K2 = omega./[(Cfsq2).^(1/2)];
K2a = K2*a;

k1 = omega./[(cfsq1).^(1/2)];
k1a = k1*a;
k2 = omega./[(cfsq2).^(1/2)];
k2a = k2*a;

nr = n2/n1; % relative viscosity
dr = d2/d1; % relative density

% Relative acoustic radii
Kk1 = k1a.*K1a;
Kk2 = k2a.*K2a;

% Scattering Coefficients
%--------------------------------------------------------------------------
for l = 0:1
    g2 = l*(l+1);
    M(l+1,1:length(f)) = [(nr-1)^2]*[g2-2];
    P(l+1,1:length(f)) = (Kk2.*drj(l,k2a).*drp(l,K2a)-g2);
    N(l+1,1:length(f)) = (1/2)*(nr-1)*((K1a).^2);
    Q(l+1,1:length(f)) = Kk1.*drh(l,k1a).*drx(l,K1a)-g2;
    U(l+1,1:length(f)) = K1a.*drx(l,K1a);
    R(l+1,1:length(f)) = k1a.*drh(l,k1a);
    T(l+1,1:length(f)) = K2a.*drp(l,K2a);
    V(l+1,1:length(f)) = k2a.*drj(l,k2a);
    W(l+1,1:length(f)) = (1/4)*((K1a).^4);
    X(l+1,1:length(f)) = g2*((1-dr)^2);
    Z(l+1,1:length(f)) = k1a.*drj(l,k1a);
    A(l+1,1:length(f)) = besselsphj(l,k1a)./hankel1(l,k1a);
    B(l+1,1:length(f)) = Kk1.*drj(l,k1a).*drx(l,K1a)-g2;

    J(l+1,1:length(f)) = T(l+1,1:length(f))+2*V(l+1,1:length(f))-2*g2;
    L(l+1,1:length(f)) = T(l+1,1:length(f))-dr*U(l+1,1:length(f));

    % Denominator of the transverse scattering coefficient
    del0(l+1,1:length(f)) = 1E-3+M(l+1,1:length(f)).*P(l+1,1:length(f)).*Q(l+1,1:length(f))+ ...
                            N(l+1,1:length(f)).*[P(l+1,1:length(f)).*(U(l+1,1:length(f))+...
                            2*R(l+1,1:length(f))-2*g2)- ...
                            dr*Q(l+1,1:length(f)).*J(l+1,1:length(f))]+ ...
                            W(l+1,1:length(f)).*[X(l+1,1:length(f))-...
                            L(l+1,1:length(f)).*(V(l+1,1:length(f))-dr*R(l+1,1:length(f)))];

    % Numerator of the transverse scattering coefficient
```

```
    del3(l+1,1:length(f)) = [K1./k1].*A(l+1,1:length(f)).*[Z(l+1,1:length(f)) - ...
                             R(l+1,1:length(f))].*[W(l+1,1:length(f))*...
                             (nr-1)*dr*(1-dr) + N(l+1,1:length(f)).*[P(l+1,1:length(f))-...
                             dr*(T(l+1,1:length(f)) + 2*V(l+1,1:length(f)) - g2)] +...
                             M(l+1,1:length(f)).*P(l+1,1:length(f))];

end

S = real(del3./del0);

%--------------------------------------------------------------------------
%--------------------------------------------------------------------------
```

Program 8.1 Lin and Raptis's dimensionless acoustic radiation force function

```
function [ F ] = linrapshear(a,Scomp,Sshear,alphamed,v)
% Lin and Raptis: Dimensionless Acoustic Radiation Force Function
% Alison Pouch  - The College of William and Mary

% Input Parameters
%--------------------------------------------------------------------------

% a = scatterer radius (m)
% Scomp = scattering coefficients of compressional wave
% Sshear = scattering coefficients of transverse wave
% alphamed = attenuation coefficient in medium (Np/m)
% v = kinematic viscosity of the medium (m^2/s)

% Other Parameters
%--------------------------------------------------------------------------

f = (2:0.01:6)*1E6;     % transducer frequency in Hz
omega = 2*pi*f;         % angular frequency in rad/s
cmed = 1570;            % acoustic speed in blood (m/s)
rho = 1060;             % density of blood (kg/m^3
K1a = (omega/cmed + f*i*alphamed*1e-6)*a;      % compressional wave number of the viscous fluid
K2a = [(1 + i)*(omega/(2*v)).^(1/2)]*a;        % viscous wave number

% Force Function
%--------------------------------------------------------------------------

F = 12*(Sshear(2,:)).*hankel1(1,K2a) - 3*[abs(Scomp(2,:)).*hankel1(1,real(K1a)) +
    besselsphj(1,real(K1a))];

%--------------------------------------------------------------------------
```

Program 8.2 Hasegawa and Yosioka's acoustic radiation force function

```
function [Y] = radforce(U,a,c)
% Hasegawa and Yosioka: Acoustic Radiation Force Function
% Alison Pouch  - The College of William and Mary

% Input Parameters
%--------------------------------------------------------------------------

% U = matrix of scattering coefficients
% a = scatterer radius (m)
% c = acoustic speed of medium (m/s)


% Other Parameters
%--------------------------------------------------------------------------

f = (0.01:0.01:6)*1E6;  % transducer frequency in Hz
kr = 2*pi*f*a/c;        % dimensionless acoustic radius

aSubn = real(U);    % real components of scattering coefficients
```

```
bSubn = imag(U);    % imaginary components of scattering coefficients


% Force Function
%--------------------------------------------------------------------------

for n = 0:49
    Yp(n+1,1:length(f)) = [-4 ./ (kr).^2] .* [(n+1) * (aSubn(n+1,:) + aSubn(n+2,:)...
            + 2 * (aSubn(n+1,:) .* aSubn(n+2,:) + bSubn(n+1,:) .* bSubn(n+2,:)))];
end

Y = sum(Yp);

%--------------------------------------------------------------------------
```